# First Results from WINERED: Detection of Emission Lines from Neutral Iron and a Combined Set of Trace Species on the Dayside of WASP-189 b

Lennart van Sluijs , <sup>1</sup> Emily Rauscher , <sup>1</sup> Eliza M.-R. Kempton , <sup>2</sup> Thomas Kennedy , <sup>1</sup> Isaac Malsky , <sup>3</sup> Noriyuki Matsunaga, <sup>4,5</sup> Michael Meyer, <sup>1</sup> Andrew McWilliam, <sup>6</sup> John D. Monnier , <sup>1</sup> Shogo Otsubo, <sup>5</sup> Yuki Sarugaku, <sup>5</sup> and Tomomi Takeuchi , <sup>5</sup>

<sup>1</sup>Department of Astronomy, University of Michigan, 1085 S. University Ave., Ann Arbor, 48109, MI, USA
<sup>2</sup>Department of Astronomy, University of Maryland, College Park, MD, USA

<sup>3</sup> Jet Propulsion Laboratory, California Institute of Technology, Pasadena, CA 91109, USA

<sup>4</sup>Department of Astronomy, School of Science, The University of Tokyo, 7-3-1 Hongo, Bunkyo-ku, Tokyo 113-0033, Japan
<sup>5</sup>Laboratory of Infrared High-resolution spectroscopy (LiH), Koyama Astronomical Observatory, Kyoto Sangyo University, Motoyama, Kamigamo, Kita-ku, Kyoto 603-8555, Japan

<sup>6</sup> The Observatories of the Carnegie Institution for Science, 813 Santa Barbara Street, Pasadena, CA 91101

### ABSTRACT

Ground and space-based observations have revealed that Ultra Hot Jupiters (UHJs,  $T_{\rm eq} > 2200$  K) typically have inverted thermal profiles, while cooler hot Jupiters have non-inverted ones. This shift is theorized due to the onset of strong optical absorbers like metal oxides (e.g., TiO, VO), metal hydrides (e.g. FeH), atomic species (e.g., Fe, Ti), and ions (e.g., H<sup>-</sup>). High-resolution spectroscopy is valuable for characterizing the thermal, chemical, and dynamical atmospheric structures due to its sensitivity to detailed spectral line shapes. The newly commissioned WINERED high-resolution spectrograph ( $R \sim 68,000$ ) on the Magellan Clay 6.5 m telescope enhances capabilities with its high throughput in the J-band (1.13-1.35  $\mu$ m), capturing strong spectral features from key atmospheric species. In this study, we report detecting the dayside atmosphere of the UHJ WASP-189 b at a  $S/N \sim 10$ , marking the first exoplanet atmosphere detection in emission with WINERED. Individually, we identify strong neutral iron (Fe) emission lines at a S/N=6.3, and tentatively detect neutral magnesium (Mg) and silicon (Si) at a S/N > 4. Although not individually detected, we detect a combined set of trace species at a S/N=7.2, which is attributed mostly to neutral chromium (Cr) and aluminum (Al), alongside magnesium and silicon. These results help refine the understanding of key atmospheric species that influence the thermal structure of WASP-189 b and UHJs more broadly.

Keywords: High resolution spectroscopy (2096), Exoplanet atmospheric composition (2021), Exoplanet atmospheric structure (2310)

### 1. INTRODUCTION

Ultra Hot Jupiters (UHJs,  $T_{\rm eq} > 2200$  K) provide an opportunity for detailed characterization of exoplanet atmospheres with current observing facilities (e.g. Fortney et al. 2021). Their presumed synchronized orbits (Rasio & Ford 1996; Showman & Guillot 2002) result in permanent day and night sides that, together with the intense stellar heating, drive strong winds and jets. High dayside temperatures allow for dissociation of both

Corresponding author: Lennart van Sluijs lsluijs@umich.edu

refractory and volatile species from molecules into their atomic and ionic counterparts. Thus, they provide an observational test bed for extreme atmospheric physics not found within the Solar System.

Hot gas giants have been successfully characterized in emission and transmission by space-based low-resolution spectroscopy using JWST and HST (e.g. Huitson et al. 2012; Sing et al. 2013; Deming et al. 2013; Spake et al. 2021; Feinstein et al. 2023; Ahrer et al. 2023; Evans et al. 2023; Coulombe et al. 2023) and ground-based high-resolution spectroscopy (HRS) (e.g. Snellen et al. 2010; Brogi et al. 2012; Birkby et al. 2013; Hoeijmakers et al. 2020; Wardenier et al. 2021; Kesseli et al. 2022; Bello-

Arufe et al. 2022; Prinoth et al. 2022; Azevedo Silva et al. 2022; Borsato et al. 2023; Gandhi et al. 2023; Giacobbe et al. 2021; van Sluijs et al. 2023; Pelletier et al. 2023). An advantage of high spectral resolution is that the individual spectral lines are resolved, and their line shape (e.g. Snellen et al. 2014; Brogi et al. 2016), wavelength offset (e.g. Snellen et al. 2010; Brogi et al. 2016; Wardenier et al. 2021; Kesseli & Snellen 2021; Gandhi et al. 2022; Pino et al. 2022; Brogi et al. 2022; Nortmann et al. 2024; Simonnin et al. 2024), and line contrast (Herman et al. 2022; Hoeijmakers et al. 2022; Pino et al. 2022; van Sluijs et al. 2023; Lesjak et al. 2024), provide a rich amount of information on the planet's chemistry, thermal structure, rotation, dynamics, and magnetism. Moreover, they encode the three-dimensional (3D) structure, that is, the regional variations as a function of height, latitude, and longitude in the atmosphere (e.g. Beltz et al. 2022, 2023; Beltz & Rauscher 2024; Wardenier et al. 2023, 2025).

Hot gas giant observations have revealed a transition around  $T_{\rm eq} \sim 1900$  K, where the cooler hot Jupiters (HJs) shift from non-inverted atmospheres, characterized by spectral absorption features, to inverted atmospheres for the UHJs, which exhibit emission features (e.g. Petz et al. 2025). This transition is theorized to occur due to the onset of strong optical absorbers such as metal oxides (e.g., TiO, VO), metal hydrides (e.g., FeH), atomic species (e.g., Fe, Ti), and ions (e.g., H $^-$ ) (e.g., Hubeny et al. 2003; Fortney et al. 2008; Arcangeli et al. 2018; Lothringer et al. 2018; Parmentier et al. 2018).

Although the observational evidence for this transition is robust, our understanding of how each optical absorber contributes is still developing. Neutral iron has been consistently detected in many exoplanet atmospheres and has been used to constrain their thermal structure (e.g., Pino et al. 2020; Yan et al. 2020; Nugroho et al. 2020; Gibson et al. 2020). There is also compelling evidence for H<sup>-</sup> as a continuum opacity source. This evidence comes indirectly from the detection of hydroxide (OH) (e.g. Nugroho et al. 2021; Landman et al. 2021) and from reduced water abundances (e.g. Mansfield et al. 2020; Gandhi et al. 2024), which are both attributed to water dissociation into OH and H<sup>-</sup>. Metal oxides, such as TiO and VO, have been conclusively detected in some hot gas giants, but results for the same planet have frequently been inconsistent (Hoeijmakers et al. 2015; Evans et al. 2016; Sheppard et al. 2017; Hoeijmakers et al. 2018; Merritt et al. 2021; Prinoth et al. 2022; Cont et al. 2022; Scandariato et al. 2023; Borsato et al. 2023; Ouyang et al. 2023; Guo et al. 2024; Hoeijmakers et al. 2024; Prinoth et al. 2025).

Cold-trapping has been proposed to explain metal oxide absence or depletion; in this scenario, titanium and vanadium-bearing species condense and sink into the deeper atmosphere on the nightside, effectively removing them from the upper parts of the atmosphere that are probed by HRS (Parmentier et al. 2013). Iron hydride (FeH) is often predicted to be observable assuming equilibrium chemistry, but despite tentative observational evidence (Evans et al. 2016), searches have not led to any conclusive detections (Kesseli et al. 2020).

The recently commissioned WINERED instrument, which has been installed at the 6.5 meter in diameter Clay/Magellan II Telescope located at Las Campanas Observatory in Chile (Kondo et al. 2015; Ikeda et al. 2022; Otsubo et al. 2024), provides a unique opportunity as its J-band (1.13-1.35  $\mu$ m) notably covers strong spectral features of metal oxides, iron hydride, iron, among other atomic and ionic species.

So far, only one published study used WINERED to constrain exoplanet atmospheres (Vissapragada et al. 2024), using the Y-band (0.96-1.11  $\mu$ m). This band covers the spectral line from the metastable state of helium at 10830 Å, which has been linked to atmospheric escape (Oklopčić & Hirata 2018). Their study with WINERED did not detect helium absorption in the transmission spectrum of the ultra-hot Neptune LTT 9779b, but instead provided an upper limit on its mass loss rate.

In addition to its suitable wavelength coverage, this spectrograph has an especially high throughput (up to about 40%) given its high spectral resolution  $(R = \lambda/\Delta\lambda_{\rm FWHM} = 68,000)$  compared to established high-resolution spectrographs that have successfully detected and characterized exoplanet atmospheres such as. e.g.: NIRSPEC (McLean et al. 1998), IRD (Kotani et al. 2018), IGRINS (Park et al. 2014; Levine et al. 2018), GIANO (Piskorz et al. 2017), CARMENES (Quirrenbach et al. 2014), iSHELL (Rayner et al. 2016), SPIRou (Thibault et al. 2012), CRIRES<sup>+</sup>, (Lavail 2021) and ARIES (McCarthy et al. 1998). Generally, the higher the spectral resolution, the more sensitive the data are to 3D exoplanet atmosphere effects, but this often comes at a cost of instantaneous wavelength coverage and instrumental throughput.

Here we present the first results from two observing nights with WINERED in HIRES-J mode targeting WASP-189 b. These observations are part of a larger survey targeting HJs over a range of irradiation temperatures and masses. WASP-189 b is a typical UHJ, first detected by the WASP-South survey using the transit method (Anderson et al. 2018). They found it orbits a

Quantity	Symbol	Value	Reference		
Stellar radius	$R_{\star}$	$2.36\pm0.03R_{\odot}$	Lendl et al. (2020)		
Stellar effective temperature	$T_{\star}$	$8000 \pm 80~\mathrm{K}$	Lendl et al. (2020)		
Primary transit time	$T_0$	$2458926.5416960^{+0.0000065}_{-0.0000064}$ (BJD)	Lendl et al. (2020)		
Eccentricity	e	$0^{a}$	Anderson et al. (2018)		
Inclination	i	$84.03 \pm 0.14 \deg$	Lendl et al. (2020)		
Orbital period	P	$2.7240338 \pm 0.0000067 \mathrm{d}$	Anderson et al. (2018)		
Planetary radius	$R_{ m p}$	$1.619 \pm 0.021  \mathrm{R_{Jup}}$	Lendl et al. (2020)		
Gravitational acceleration	g	$18.8^{+2.1}_{-1.8} \text{ m/s}$	Lendl et al. (2020)		
Dayside equilibrium temperature	$T_{ m p}$	$3353^{+27}_{-34}\mathrm{K}$	Lendl et al. (2020)		
System velocity	$V_{ m sys}$	$20.82 \pm 0.07$	Yan et al. (2020)		
Keplerian velocity	$K_{ m p}$	$197^{+15}_{-16}{ m km/s}^{b}$	Anderson et al. (2018)		

**Table 1.** An overview of relevant stellar and planetary parameters, demonstrating WASP-189 b is a typical ultra hot Jupiter.

fast-rotating (line-of-sight velocity of  $\sim 100$  km/s) hot F-star ( $T_{\star} \sim 8000$  K) on a polar orbit. Its orbital, stellar, and planetary parameters have been further accurately constrained by CHEOPS follow-up observations (Lendlet al. 2020; Deline et al. 2022, see Table 1).

A few HRS studies have observed WASP-189 b to characterize its atmosphere. Yan et al. (2020) used HARPS-N in the optical to search for a range of atoms and ions. They were the first to report neutral iron emission lines in the dayside atmosphere of WASP-189 b, indicating an inverted thermal structure. Analysis of transmission spectra taken by HARPS, HARPS-N, ESPRESSO and MAROON-X have revealed TiO, Ti, Ti<sup>+</sup>, Fe, Fe<sup>+</sup>, Cr, Mg, V, Mn, Na, Ca, Ca<sup>+</sup>, V, Mn, Ni, Sr, Sr<sup>+</sup>, and Ba<sup>+</sup> (Stangret et al. 2022; Prinoth et al. 2022, 2023, 2024). Further emission HRS studies have confirmed neutral iron emission in the optical (Deibert et al. 2024) on the dayside and also detected carbon monoxide in the near-infrared (Yan et al. 2022; Lesjak et al. 2025).

In addition, NUV transmission spectroscopy observations at lower resolution (10-100 Å) with CUTE (Sreejith et al. 2023) detect Mg II and find evidence for Fe II in WASP-189 b. They also revealed an extended upper atmosphere beyond the Roche lobe at a significantly higher temperature ( $\sim 15,000~\rm K$ ) than predicted from hydrodynamical models. This is consistent with Non-Local Thermal Equilibrium (NLTE) chemistry in the upper atmosphere of WASP-189 b. Modeling of hot Jupiters has shown NLTE effects can alter the chemistry and thermal conditions of their upper atmospheres

(e.g. Young et al. 2020; Wright et al. 2022) with observational signatures mainly in transmission, but also in emission spectra (e.g. Barman et al. 2002; Swain et al. 2010; Moses et al. 2011; Fossati et al. 2021; Borsa et al. 2021; Young et al. 2024). HJs commonly orbit early-type A and F stars (Casasayas-Barris et al. 2019), where varying XUV flux environments can further enhance atmospheric photo-ionization (Fossati et al. 2018). WASP-189 b orbits an early type F-star, which likely increases photo-ionization affecting the abundance of ionic species in its atmosphere.

This manuscript is structured in the following way. Section 2 discusses our observational strategy and data processing. Section 3 describes how our atmospheric modeling is used to compute spectral templates. Section 4 explains how we combined our reduced data and spectral templates via HRS cross-correlation methodology for atmospheric characterization. Section 5 presents the results of this analysis. Section 6 contains the discussion of these results. Finally, Section 7 presents the main findings and some ideas for future research.

# 2. OBSERVATIONS AND DATA PROCESSING

### 2.1. Observations

We observed our target WASP-189 for two nights using the 6.5 m Clay/Magellan II Telescope located at Las Campanas Observatory in Chile. An overview of the observing setups for both nights is shown in Table 2. The setup for the two nights differs slightly as

 $<sup>^</sup>a\mathrm{Assumed}$  by Anderson et al. (2018) while fitting for the transit shape.

<sup>&</sup>lt;sup>b</sup>Computed from the orbital parameters assuming a Keplerian orbit.

Table 2.	An	overview	of	the	observing	$\operatorname{setup}$	and	conditions	for	both
nights.										

${\bf Quantity}$	Night 1	Night 2
$UT_{ m start}$	2023-06-08 22:50	2024-04-20 00:18
$UT_{\mathrm{end}}$	2023-06-09 02:45	2024-04-20 09:42
Instrument mode	HIRES-J	HIRES-J
Slit width $[\mu m]$	100	100
Phase coverage	0.42 - 0.48	0.47 - 0.59
Number of frames	125	268
Exposure time [s]	$50/60^{a}$	60
Nodding pattern	ABBA	AB
Median humidity [%]	13.7	18.2
Median S/N per frame pair	222	186
Median FWHM [pixel]	4.6	5.1

<sup>&</sup>lt;sup>a</sup>Started with 60 s exposures, but changed to 50 s to avoid detector saturation.

we optimize it for HRS of exoplanet atmospheres with WINERED, which is discussed in more detail throughout this section. In both cases, the instrumental mode used was HIRES-J in combination with a 100  $\mu$ m slit. This covers wavelengths from 1.13-1.35  $\mu$ m at a spectral resolving power of  $\sim 68,000$  (Ikeda et al. 2022).

Combining both nights, our observations cover orbital phases from pre- to post-eclipse (see left panel of Fig. 1). We also observed during the secondary eclipse, since WINERED observing time is allocated nightly. Even though the atmospheric signal of WASP-189 b is obscured by the star during the secondary eclipse, these observations are still useful. They help confirm that the exoplanet signal has disappeared, which aids in distinguishing between actual atmospheric signals and stellar signals or systematic errors.

For each observing night, calibration images were obtained in the morning using the same instrument mode and slit width. This was done following the standard calibration procedure described by Hamano et al. (2024). First, flat fields are taken from the flat screen without illumination, and then the same images are taken with lighting. Then, flat fields are taken, imaging multiple pinholes. Lastly, a ThAr lamp was used for wavelength calibration of the slits.

The exposure time used differed between the first and second night. During the first night, we started with an exposure time of 60 s, but decided to change it to 50 s to avoid detector saturation towards the end of the observations. This was due to the excellent seeing conditions during that night, and affects 27 frames in to-

tal. However, only 4 frames were before the secondary eclipse, mitigating its impact on exoplanet atmospheric detection. During the second night, we used a 50 s exposure time from the start instead. All of the exposure times were in the photon-limited regime, as computed using WINERED's Exposure Time Calculator<sup>1</sup>. Occasionally, the WINERED instrument tracking software disconnected. In those cases, we had to manually recenter and track the target, after which, observing continued.

Alongside the exposure time, a different nodding pattern was used for each night. The first night used an ABBA nodding pattern. This is a standard nodding pattern used for most HRS exoplanet observations, as it reduces the overhead due to the few seconds it takes in between exposures to nod from slit position A to B. This works well when subsequent exposures at the same slit position are independent. However, this is not necessarily warranted in the case of WINERED, as the NIR detector suffers from persistence. This effectively creates a ghost image of each previous exposure that decays over time. Especially, the persistence of a bright target can be significant in the following exposures of a fainter target. Therefore, exposing twice at the same nodding position can result in an asymmetric persistence signal. Although the persistence of the target itself is expected to be small for many applications, we decided

https://merlot.kyoto-su.ac.jp/WINERED/ETC/calc\_obstime.php

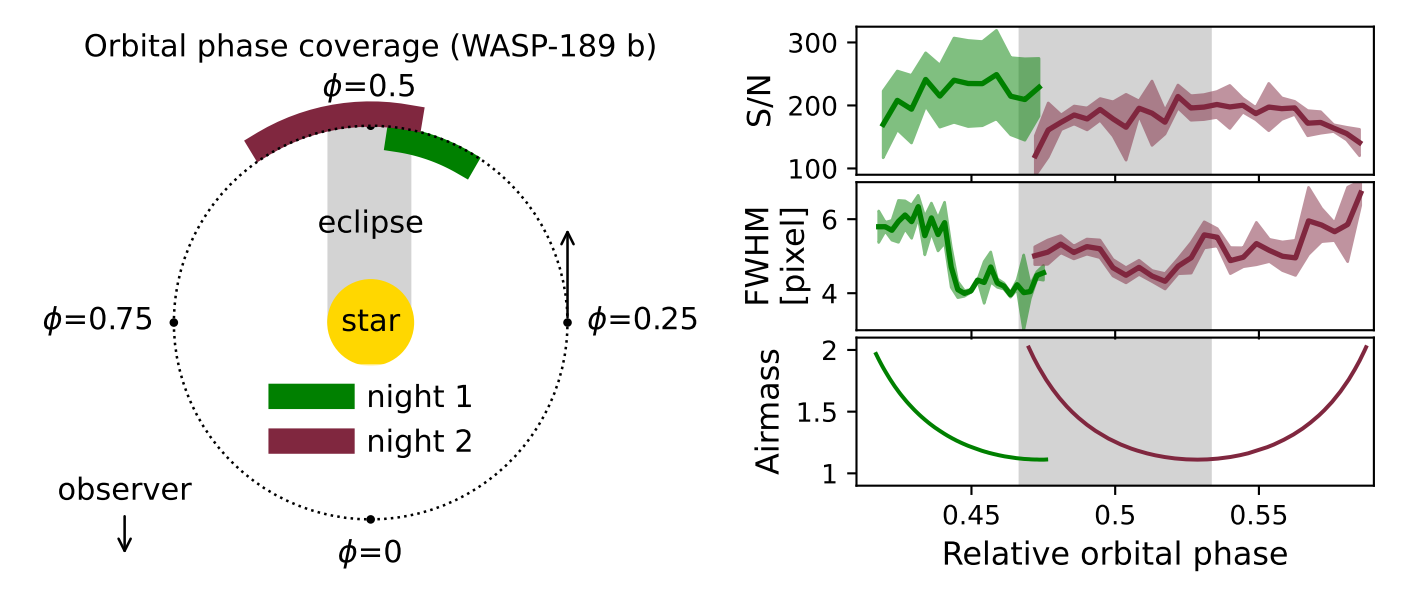


Figure 1. Left panel: Phase coverage of WASP-189 b's orbit during our two observing nights. The orbit of WASP-189 b is shown face-on (dotted black line), with the observer's direction indicated. Relative orbital phases ( $\phi$ ) are annotated along quarterly intervals. The first (green) and second (wine red) nights cover the pre-eclipse and post-eclipse phases. Both nights cover (part of) the secondary eclipse. Right panel: Time series of three observables: the signal-to-noise rate per frame pair (S/N), Full Width Half Maximum of the trace on the detector (FWHM in pixel), and airmass are shown. The same colors as in the left panel are used to indicate each night. The time series has been binned (ten frames per bin), and the standard deviation of each bin is plotted as the shaded region.

to mitigate its potential risk, considering the high S/N we would like to achieve. This was done by using an AB nodding pattern during the second night, which has a regular time interval between exposures taken at the same slit position. We come back to this point in Section 2.3.

## 2.2. Data processing

The raw detector images for both nights were pre-processed using WINERED's processing pipeline WARP, which has been made publicly available by the instrument team and is described in more detail in Hamano et al. (2024). We used the default input parameters set by the pipeline. The HIRES-J mode covers 22 spectral orders, namely m = 131 - 153. We extracted raw spectra over 1.3 times the free spectral range for each spectral order. The pipeline does a bias and dark correction, flat-field correction, and sky subtraction. It then measures the FWHM of the traces on the detector and extracts the raw spectra from the echelle apertures. Alongside the extraction of the raw spectra, the pipeline also produces normalized spectra where a continuum has been fitted and the raw spectra are divided by the fit. The differences between the two spectra are used to compute the continuum S/N per frame pair.

The pipeline also includes a wavelength alignment and calibration step, where cross-correlation is used to align and calibrate spectra in the spectral time series.

The data was further post-processed using our pipeline, which we make available on GitHub<sup>3</sup>. This pipeline performs the following steps (see Fig. 2):

- Spectral time series extraction: A multidimensional data cube is created from the WARP output directory. This is done by combining all normalized, wavelength-calibrated spectra of all spectral orders. This data cube thus has the following dimensions: number of frames × number of spectral channels × number of spectral orders.
- 2. Orbital phase calculation: All times are extracted from the FITS headers and converted from Julian Date (JD) to barycentric Julian Date (BJD). We use the ephemeris and period of WASP-189 b listed in Table 1 to compute the relative orbital phase, assuming a circular orbit (following assumptions by Anderson et al. 2018; Lendl et al. 2020).
- 3. Artificial injection: following van Sluijs et al. (2023), an artificial exoplanetary signal can op-

<sup>&</sup>lt;sup>2</sup> https://github.com/SatoshiHamano/WARP

<sup>&</sup>lt;sup>3</sup> https://github.com/lennartvansluijs/WINERED

# Spectral time series (order=141)

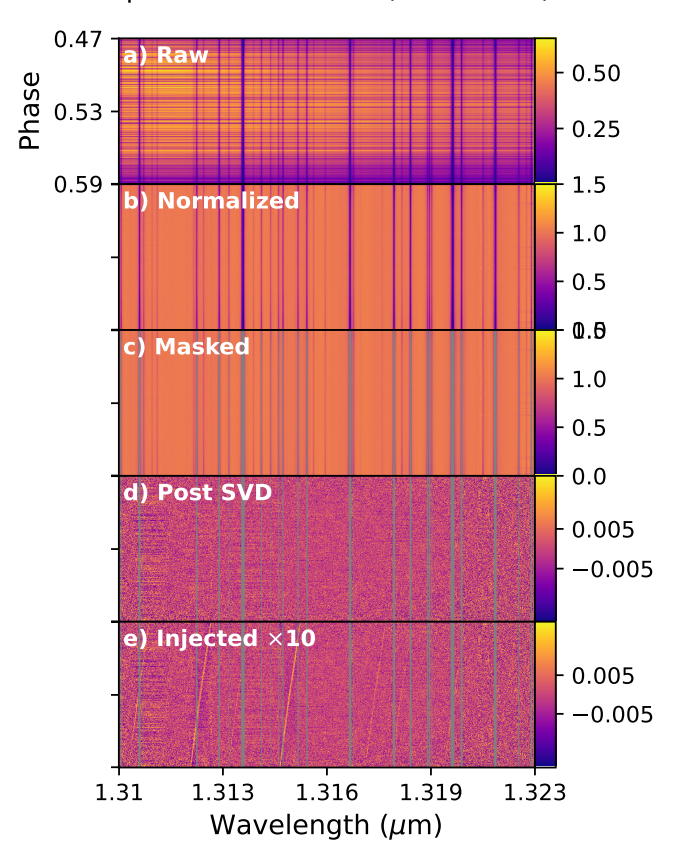


Figure 2. Example of processing a spectral time series for the 141st spectral order and the second night. The color bar indicates photon counts, normalized to an appropriate value for each panel: (a) the raw spectral time series is normalized to its maximum value. (b) the spectral time series normalized to the continuum. (c) the same as in panel 2, but with the strongest telluric features masked, and shown in gray. (d) Post removal of the quasi-stationary components by SVD. (e) the same as in panel 4, but with the fiducial model injected at ten times the nominal star-to-planet flux ratio. The strongest emission lines are visible as bright sloped lines, blue-shifting due to the planet's orbital acceleration.

tionally be injected at this stage. This is useful to test the sensitivity to different atmospheric models of WASP-189 b for these observations. This is done by multiplication of the normalized spectral time series by  $a \times (1 + F_{\text{scaled}})$ , where  $F_{\text{scaled}}$  is a scaled spectral template Doppler-shifted to the exoplanet's expected radial velocity (discussed in Section 4), and a an additional scale parameter (introduced by Brogi & Line (2019)).

4. Telluric masking: strong telluric lines are commonly masked in HRS post-processing, as they are difficult to sufficiently remove from the spectra

(e.g. Spring et al. 2022; van Sluijs et al. 2023). We mask spectral channels with a continuum flux below a threshold of 70%. This threshold is a trade-off between excluding the spectral regions contaminated by the strongest telluric lines, while retaining broad wavelength coverage essential for robust signal extraction.

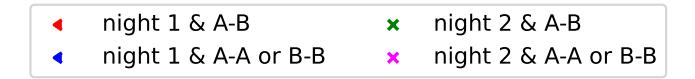
5. Removal of the quasi-stationary components: we use Singular Value Decomposition (SVD) of the spectral time series for each spectral order to remove the quasi-stationary telluric, stellar, and systematic components. The detection S/N varies with the number of removed components; however, section A and Fig. 12 of the appendix show that our key results remain robust despite slight changes in this number. Therefore, we fixed the number of removed components to seven in the remainder of this work.

The residual spectral time series are the continuumremoved exoplanetary spectra buried in the photon-shot noise. These spectra will be used in the subsequent cross-correlation analysis.

## 2.3. Observed instrumental performance

The time series of a selection of relevant observables is shown on the right side of Fig. 1. These are the S/N per frame pair, FWHM of the echelle traces, and airmass are shown as a function of relative orbital phase. As expected, the S/N is broadly inversely correlated to the airmass. The standard deviation of the S/N is larger during the first night compared to the second night. A jump in the FWHM is visible during the first observing night, which corresponds to a change in the observing seeing conditions. During the first night, the median S/N per frame is 222, slightly higher than during the second night, which is 186. During the first night, the median humidity was 13.7%, within the normal range for Las Campanas Observatory. Unfortunately, the median humidity was not recorded during the first night in the file headers, due to a broken link between the instrument and the telescope systems. However, we did recover the humidity from the weather archive of Las Campanas Observatory<sup>4</sup>. The median humidity was slightly higher at 18.2%. This is supported by the depth of the normalized telluric lines, which are visually deeper during the second night compared to the first night (see Fig. 13 of the appendix).

<sup>4</sup> https://weather.lco.cl/clima/weather/Magellan/ weathercalendar.html



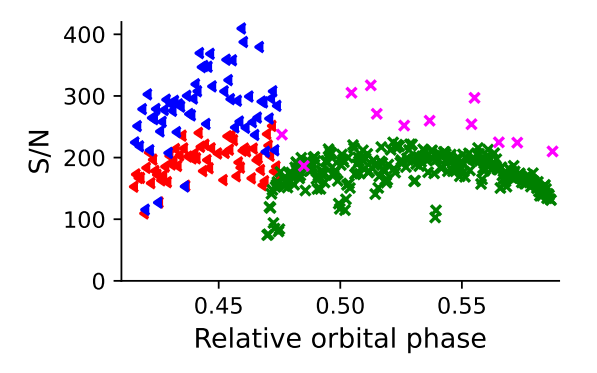


Figure 3. Signal-to-noise ratio (S/N) per frame pair. Triangles pointing to the left indicate frame pairs observed during the first night, and crosses mark the second night. Blue and magenta colors indicate homogeneous pairs, whereas red and green colors indicates heterogeneous combinations. A clear pattern emerges, where the average S/N is higher for homogeneous pairs. We prefer a more stable S/N because our post-processing algorithm can more easily remove quasistationary components.

We investigate whether the difference in standard deviation of the S/N between the first and second nights is due to the different nodding patterns of ABBA and AB, respectively. To explore this, we created two groups: one with A-B pairs and one containing both A-A and B-B pairs. These two groups show two distinct trends in the S/N time series, as seen in Fig. 3. Due to interruptions of some exposures, a few consecutive frame pairs were taken at the same slit position during the second night, despite having adopted an AB nodding pattern.

Generally pairs taken at the same slit position correlate with a higher S/N value. We speculate three reasons this may be the case. First, it may indicate signal accumulating due to detector persistence when consecutive exposures that are taken at the same slit position. However, it is unlikely persistence alone can explain the magnitude of these effects; the magnitude of the change in S/N is far greater than the effect of persistence as measured from the raw detector images, which is on the order of a few percent. Second, it may be due to systematic errors related to the flat field correction between different nodding positions. Third, it may be due to small pointing offsets after nodding between slit position A and B. Generally, for HRS, a stable S/N is favored, as this improves the removal of quasi-stationary components during SVD. Therefore, we recommend future HRS exoplanet observations with WINERED using

AB nodding over ABBA, albeit at a slight cost of extra overhead time to nod between slit positions.

#### 3. ATMOSPHERIC MODELING

Spectral templates need to be computed using atmospheric modeling to compare against the observed spectra, utilizing cross-correlation. We used the PETITRADTRANS radiative transfer code to compute spectral templates. This code performs radiative transfer by splitting the atmosphere into a stack of atmospheric layers. Our atmospheric model consists of 100 logarithmically equally spaced pressure layers between  $10^{-8}$  and  $10^2$  bar. Each layer has a specified pressure, temperature, mean molecular weight (MMW), and chemical abundances. We adopt the pressure-temperature (P-T) profile observationally constrained by Yan et al. (2020).

We compute two sets of spectral templates: (1) assuming chemical equilibrium and (2) assuming artificially high chemical abundances. In the chemical equilibrium case, the MMW and chemical abundances are computed using the FastChem chemical network code (Stock et al. 2018). This code assumes solar elemental abundances from (Asplund et al. 2009), and equilibrium chemistry to compute chemical abundances as a function of pressure. An overview of the assumed P-T profile, MMW, and chemical abundances is shown in Fig. 4. We use a constant gravity of  $q = 18.8 \text{ m/s}^{-2}$  (Lendl et al. 2020). In line with observational constraints of the host star, we assume a  $1 \times$  solar metallicity atmosphere (Anderson et al. 2018). In the high chemical abundance case, the chemical abundances are artificially raised to  $\log VMR = -4$ . This is particularly useful to search for opacity sources where equilibrium chemistry predicts low chemical abundance, but that still have strong spectral features in the J-band (e.g. H<sub>2</sub>O, FeH).

We explore spectral templates containing one of the following opacity sources: CO (Rothman et al. 2010), H<sub>2</sub>O (Polyansky et al. 2018), OH (Yousefi et al. 2018), K, Na, (both from VALD, Allard wings, see Mollière et al. (2019)), FeH (Wende et al. 2010), TiO (McKemmish et al. 2019), VO (Bowesman et al. 2024), Fe, Fe<sup>+</sup>, V<sup>+</sup>, V, Ti<sup>+</sup>, Ti, Ca, Ca<sup>+</sup>, Si, Mg, Mg<sup>+</sup>, Cr, N, and Al (all by Kurucz<sup>5</sup>). All include collision-induced absorption from H-He (Borysow et al. 1988, 1989; Borysow & Frommhold 1989) and H-H (Borysow et al. 2001; Borysow 2002). The opacity sources were selected primarily based on their spectral features within the J-band and availability in PETITRADTRANS. Exceptions were VO, Ti<sup>+</sup>, whose latest line lists were unavailable in the

<sup>&</sup>lt;sup>5</sup> http://kurucz.harvard.edu/

# Fiducial model of WASP-189 b: thermal and chemical profiles

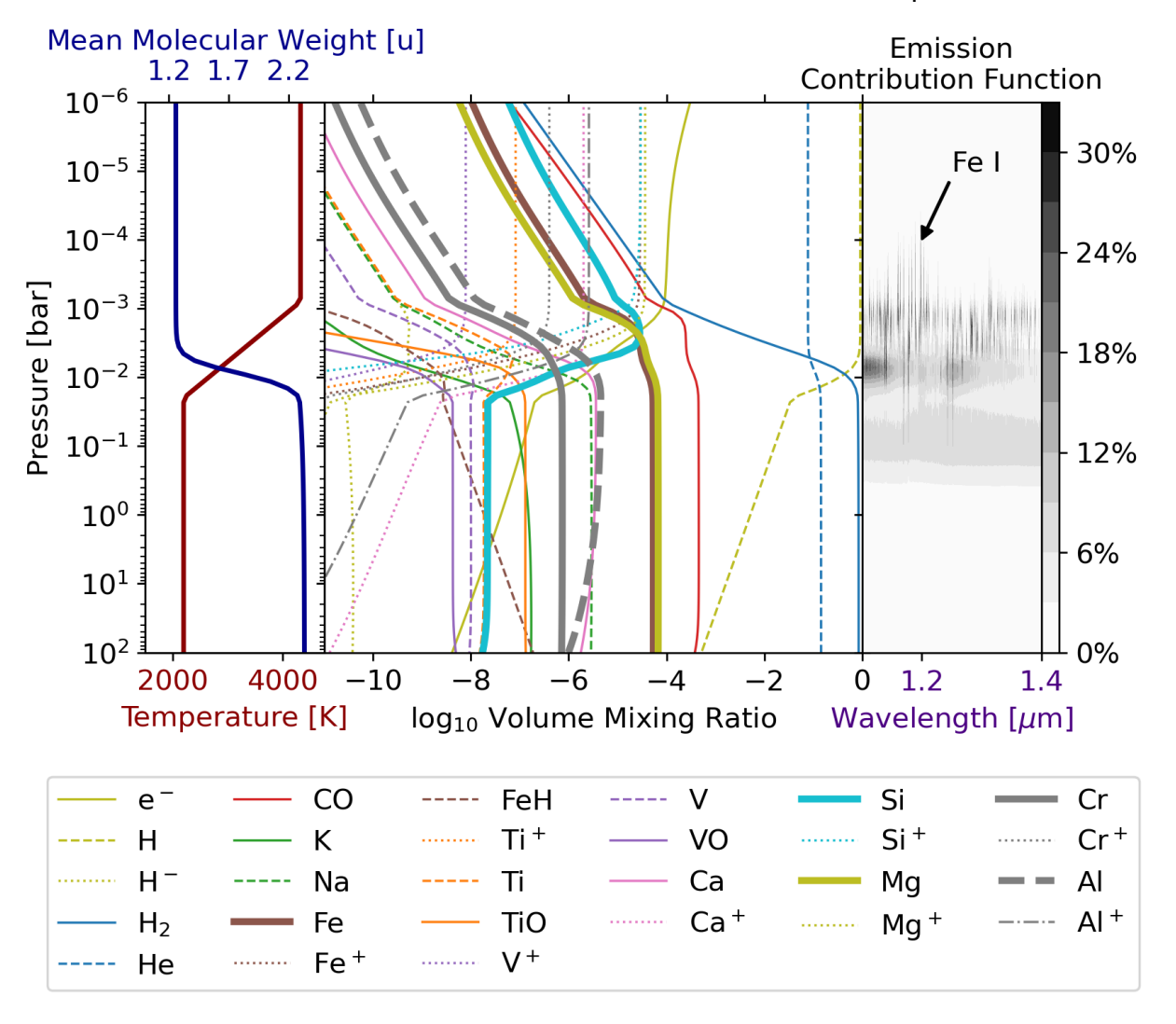
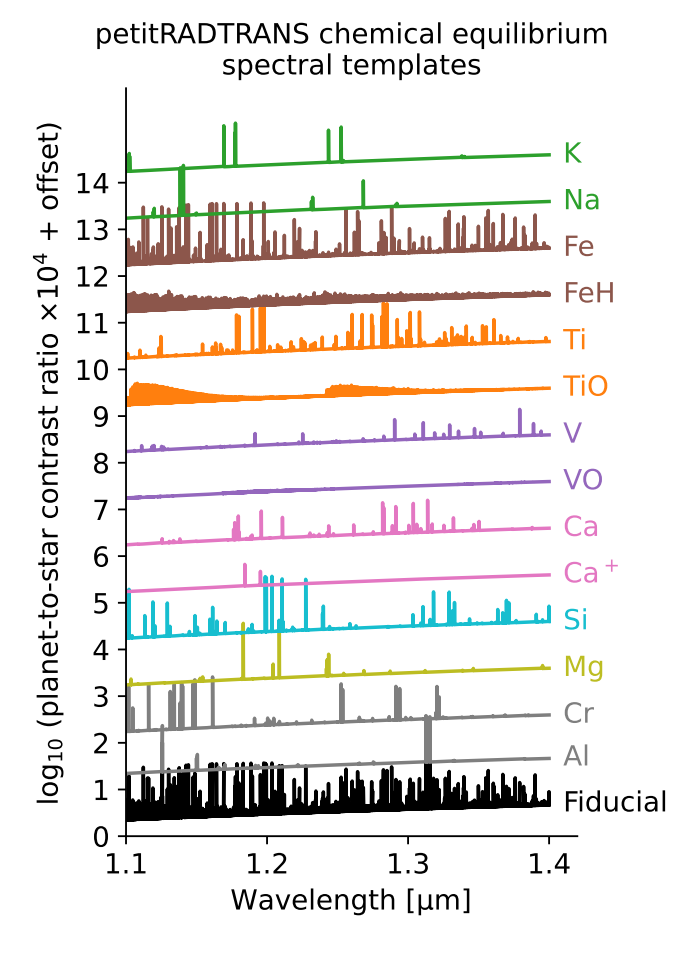


Figure 4. Temperature, MMW, and VMR as a function of pressure for the chemical equilibrium model of WASP-189 b. The P-T profile comes from Yan et al. (2020). The MMW and VMR values have been computed from the P-T profile using the FASTCHEM chemical equilibrium solver, assuming solar elemental abundances. For visual purposes we plot a selection of those most relevant to this work, although chemical abundances of additional atmospheric species were computed with FASTCHEM and included in the MMW. Left panel: P-T and MMW profiles. Middle panel: VMRs for the species shown in the legend on the right. The chemical profiles most relevant to this work (Fe, Si, Cr, Al) have been highlighted using a thicker line width. Right panel: the Emission Contribution Function for the fiducial spectral template. A spectral line core of neutral iron is highlighted, which forms at pressures of  $\sim 0.1-1$  mbar.

PETITRADTRANS format. We acquired the latest hyVO line list through private communication (see acknowledgments) and used the POSEIDON (MacDonald & Madhusudhan 2017; MacDonald 2023) radiative transfer code for Ti<sup>+</sup>, retaining the same P-T structure and chemical profile. Alongside spectral templates with a single opacity source, we also computed a fiducial spectral template that includes all opacity sources assuming equilibrium chemistry. Additionally, templates with

one opacity source removed from the fiducial model were computed.

Fig. 5 shows the computed equilibrium chemistry spectral templates for the fiducial model and for those with a single opacity source included. The plots exclude the equilibrium chemistry spectral templates for N, H<sub>2</sub>O, CO, Ti<sup>+</sup>, Mg<sup>+</sup>, Fe<sup>+</sup> and V<sup>+</sup>, since their spectra were featureless, and we excluded these spectral templates from further analysis in this work. The figure shows neutral titanium and iron have a large num-



**Figure 5.** Equilibrium chemistry spectral templates computed using PETITRADTRANS for the fiducial and single-specie models over WINERED's J-band. These spectral templates do not include  ${\bf H}^-$  as a continuum opacity source. Spectra are offset by unity on the y-scale. Neutral iron has many strong lines and is prevalent in the fiducial model.

ber of strong lines in the J-band, enhancing their potential detectability. TiO, FeH, and VO have a dense forest of weaker spectral lines. The other atmospheric species range from a few to a moderate number of strong lines. Finally, to understand the pressure range probed, we computed the emission contribution function for the fiducial spectral template with PETITRADTRANS (see right panel of Fig. 4). We find typical pressures probed by neutral iron line cores are between 0.1-1 mbar, whereas the continuum forms at deeper pressures around 1 bar.

### 4. CROSS-CORRELATION METHODOLOGY

To detect atmospheric species in WASP-189 b we use the signal-to-noise (S/N) method described in detail by van Sluijs et al. (2023), and which we briefly summarize here.

1. Model scaling relative to the star: The spectral template is scaled to the expected planet-to-star contrast ratio using

$$F_{\text{model,scaled}} = \frac{F_{\text{model}}}{B_{\star}} \left(\frac{R_{\text{p}}}{R_{\star}}\right)^{2},$$
 (1)

where  $F_{\rm model}$  is the spectral template,  $B_{\star}$  a black body curve at the stellar temperature,  $R_{\rm p}$  the planet's radius and  $R_{\star}$  the stellar radius. The division by a black body at the stellar temperature instead of a stellar atmospheric model is warranted by the hot temperature ( $\sim 8000~{\rm K}$ ), and fast rotation ( $\sim 100~{\rm km/s}$ ) of the host star, suppressing strong stellar spectral features.

- 2. Spectral resolving power: Each spectral template is convolved to WINERED/HIRES-J's spectral resolution of R=68,000.
- 3. Cross-Correlation Function: The residual spectra are cross-correlated against the scaled spectral template for a range of Doppler shifts. We explore a grid of radial velocity offsets between -500 and 500 km/s in steps of 4.4 km/s, set by the spectral resolving power of WINERED/HIRES-J
- 4. Trial rest frames: the Cross Correlation Function (CCF) time series is shifted for a range of trial orbital solutions. We assume a circular orbit, following assumptions by Anderson et al. (2018) and Lendl et al. (2020). We explore a grid of system velocities between -50 and 50 km/s and Keplerian velocities between 100 and 300 km/s. For each trial velocity, we shift to the planet's trial rest frame and add the sum of all the CCFs for each spectral order.
- 5. Spectral order weighting: To combine the CCF time series of all spectral orders, we use a modeldependent weighting scheme. This is necessary for two reasons. First, some spectral templates only have spectral features in certain spectral orders. This is particularly noticeable, for example, in the case of potassium and sodium, which only have a few strong lines in a few of the spectral orders (see Fig. 5). Second, the telluric, stellar, and systematic residuals differ per spectral order, and they will not be equally sensitive to an exoplanetary signal. Following van Sluijs et al. (2023), we use injection-recovery to measure the CCF signal in each of the spectral orders. This is done by computing the residual CCF in the planet's rest frame between the observed data and injected data

(third step of section 2.2) at an offset radial velocity of  $\Delta v_{\rm sys} = \Delta K_{\rm p} = -30$  km/s and a nominal planet-to-star flux ratio, thus a=1. Spectral orders are then weighted according to the strength of the peak residual CCF relative to other spectral orders.

6. S/N calculation: The S/N ratio is calculated by dividing the combined CCF's standard deviation from the signal in the trial planet's rest frame for each  $v_{\rm sys}$  and  $K_{\rm p}$  combination.

For detected species (S/N>5), we estimate  $v_{\rm sys}$  and  $K_{\rm p}$  uncertainties from the  $SNR_{\rm peak}-1$  contour levels. To measure rotational broadening  $\delta v_{\rm broad}$ , we also fit a Gaussian to the summed CCF in the planet's rest frame. For those spectral templates with a sufficiently high S/N, the Doppler trail will be visible directly in the CCF time series. In these cases, we will bin the cross-correlation time series into a suitable number of smaller bins and fit a Gaussian profile to each one. The maximum of the Gaussian corresponds with an average velocity offset for those orbital phases within the bin.

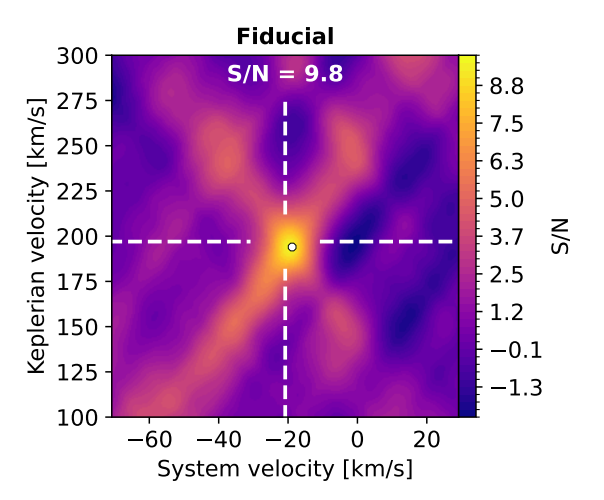
## 5. CROSS-CORRELATION RESULTS

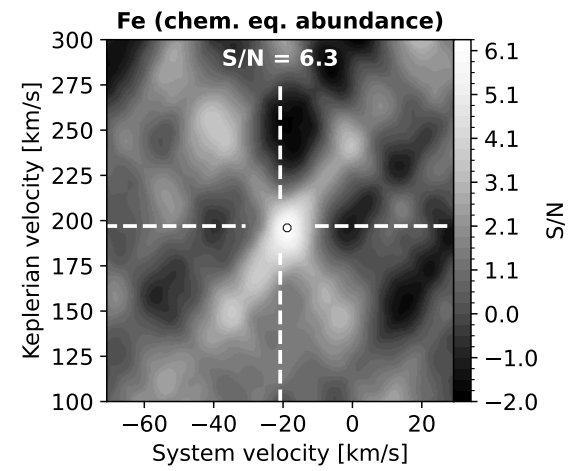
# 5.1. S/N maps

The S/N maps with detections are shown in the panels of Fig. 6. The same maps are shown for each night separately in Fig. 14 of the appendix. They show a significant detection of the atmosphere of WASP-189 b (fiducial model is detected at S/N = 9.8), and neutral iron (S/N = 6.3). These detections are well above the limit for which correlated noise in these types of S/N-maps is known to stochastically cause false positives S/N < 4 (Cabot et al. 2020; Spring et al. 2022). Our peak S/N-value is also significantly higher than the absolute minimum value in both maps, which indicates it is unlikely to be caused by correlated noise.

The location in the S/N maps aligns well with the literature values  $v_{\rm sys}=20.82\pm0.07$  km/s (Yan et al. 2020) and  $K_{\rm p}=197^{+15}_{-16}$  km/s (Anderson et al. 2018). For the fiducial model we find  $v_{\rm sys}=-19.5^{+2.4}_{-2.6}$  km/s and  $K_{\rm p}=194^{+7}_{-6}$  km/s, and for the iron-only model we find  $v_{\rm sys}=-19.0^{+3.1}_{-2.0}$  km/s and  $K_{\rm p}=195^{+8}_{-9}$  km/s. For the fiducial model, we find  $\delta v_{\rm broad}=6.1\pm0.4$  km/s and for the iron-only we find  $\delta v_{\rm broad}=5.4\pm0.2$  km/s

The  $v_{\rm sys}$  versus  $K_{\rm p}$  maps for our other spectral templates are shown in the appendix: Fig. 15 shows the non-detected species assuming chemical equilibrium, and Fig. 16 shows all species assuming high chemical abundance (log VMR=-4). Except for the high chemical abundance iron-only template, all of these are below our tentative detection limits of S/N<4. The only excep-





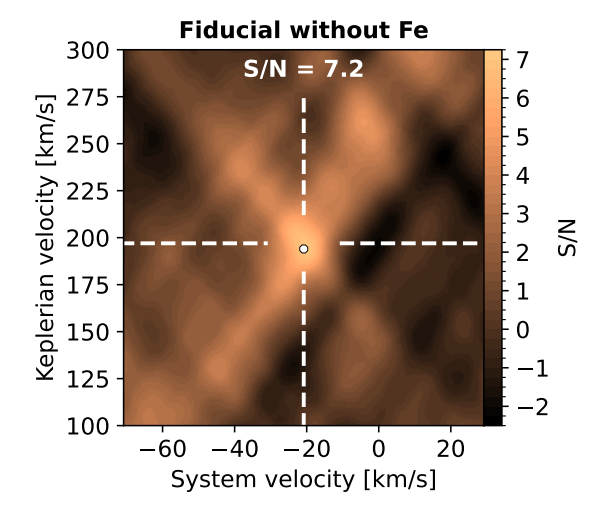


Figure 6. S/N as a function of system velocity  $(v_{\rm sys})$  and Keplerian velocity  $(K_{\rm p})$  when combining all out-of-eclipse phases for both nights in the barycentric rest frame. The literature values for  $v_{\rm sys}$  and  $K_{\rm p}$  are indicated by the white dashed cross. The maximum S/N is marked by the small circle, and its value is annotated at the top of the plot. Top left: for the fiducial spectral template Top left: for the neutral iron (Fe) spectral template using the chemical profile assuming equilibrium chemistry. Bottom: the fiducial spectral template without neutral iron.

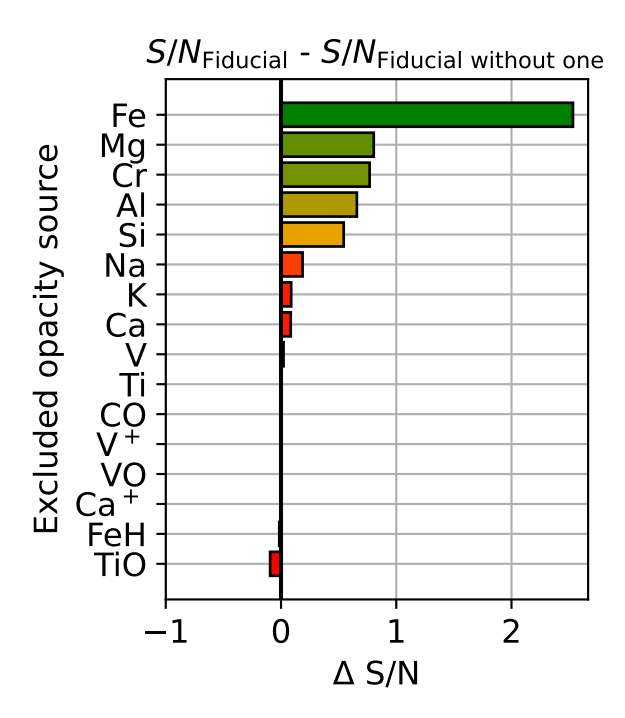


Figure 7. Differences in signal-to-noise ratio  $(\Delta S/N)$  are measured between the complete fiducial spectral template and templates omitting one opacity source at a time. Large positive  $\Delta S/N > 1$  values indicate a significant detection of the excluded opacity source (e.g., Fe), whereas near-zero values suggest that excluding or including the opacity source has little effect, indicating insignificant detection.

tion is silicon (Si), which is tentatively detected at a S/N = 4.1.

Despite the non-detections of other species than iron, the fiducial model is detected significantly higher than the iron-only model, suggesting a contribution from a subset of the other atmospheric species. To investigate this further, we also cross-correlated the data against the fiducial spectral template that excluded a single atmospheric species. The difference in S/N-ratios is shown in Fig. 7. Excluding iron significantly reduces the detection S/N by about two, indicating its presence in the atmosphere. The exclusion of other species reduces the detection S/N slightly, but by less than one, indicating an insignificant presence or absence. To check if their combined contribution is significant, we also cross-correlated with a fiducial spectral template with iron excluded. This template is significantly detected around WASP-189 b's expected  $v_{\rm sys}$  and  $K_{\rm p}$  location at a S/N = 7.2 (see bottom right of Fig. 6). Thus, the combined contribution of all opacity sources other than iron is significant, despite insignificant detections for each of these species individually. Fig. 7 shows that this can mainly be attributed to a combination of magnesium (Mg), chromium (Cr), aluminum (Al), and silicon (Si).

# 5.2. Doppler trails

The Cross-Correlation Function (CCF) time series is shown for the fiducial model in Fig. 8. This figure includes orbital phases observed during the secondary eclipse, which were excluded from the S/N calculation. In the top panels, a peak in the CCF time series, the Doppler trail, can be seen in the pre-eclipse data, disappears during the secondary eclipse, and reappears in the post-eclipse data. This becomes more significant when summing up the CCF during these different orbital phase intervals (bottom panel). This provides unambiguous evidence that the signal originates from WASP-189 b and is not due to telluric, stellar contamination, or systematics. The post-eclipse trail is clearer than the pre-eclipse, and this is reflected by the higher detection S/N during the second night (see Fig. 14 of the appendix). We speculate this may be due to the higher stability of the continuum S/N (see Fig. 1) compared to the first night.

We applied the Gaussian fitting to the spectral templates with iron only, the fiducial template, and the fiducial template without iron. Three bins were used precelipse and post-eclipse. Our alternative orbital fit is shown in the literature planet rest frame in Fig. 9. If our study of WASP-189 b had found the same  $v_{\rm sys}$  and  $K_{\rm p}$  values as the literature, all points should follow a vertical line at a net-zero velocity offset. However, our  $v_{\rm sys}$  and  $K_{\rm p}$  values differ slightly from the literature value from Anderson et al. (2018), thus our best alternative fit has a slight slope in Fig. 9. Although this is consistent with the literature value within our measured error on  $v_{\rm sys}$  and  $K_{\rm p}$ , as indicated by the shaded region, it may also hint towards 3D effects, which we get back to in Section 6.4.

# 6. DISCUSSION

## 6.1. Iron detection

Our detection of neutral iron in the atmosphere of WASP-189 b is the first detection in the J-band. The detection of iron is compatible with equilibrium chemistry, which predicts a relatively high chemical abundance ( $\log_{10} X_{\rm Fe} \sim -5$ ) around line-forming pressures ( $P \sim 10^{-3} - 10^{-5}$  mbar). The detection of neutral iron emission lines independently confirms a temperature inversion in the atmosphere of WASP-189 b. This agrees with the observed trend that UHJs have inverted dayside atmospheres (e.g. Petz et al. 2024). Our iron detection is consistent with previous observations from other instruments, including HARPS-N (Yan et al. 2020), CRIRES+ (Lesjak et al. 2024), GHOST (Deibert et al. 2024). Therefore, this work contributes to an emerging trend that iron is detectable in UHJ atmospheres across a wide

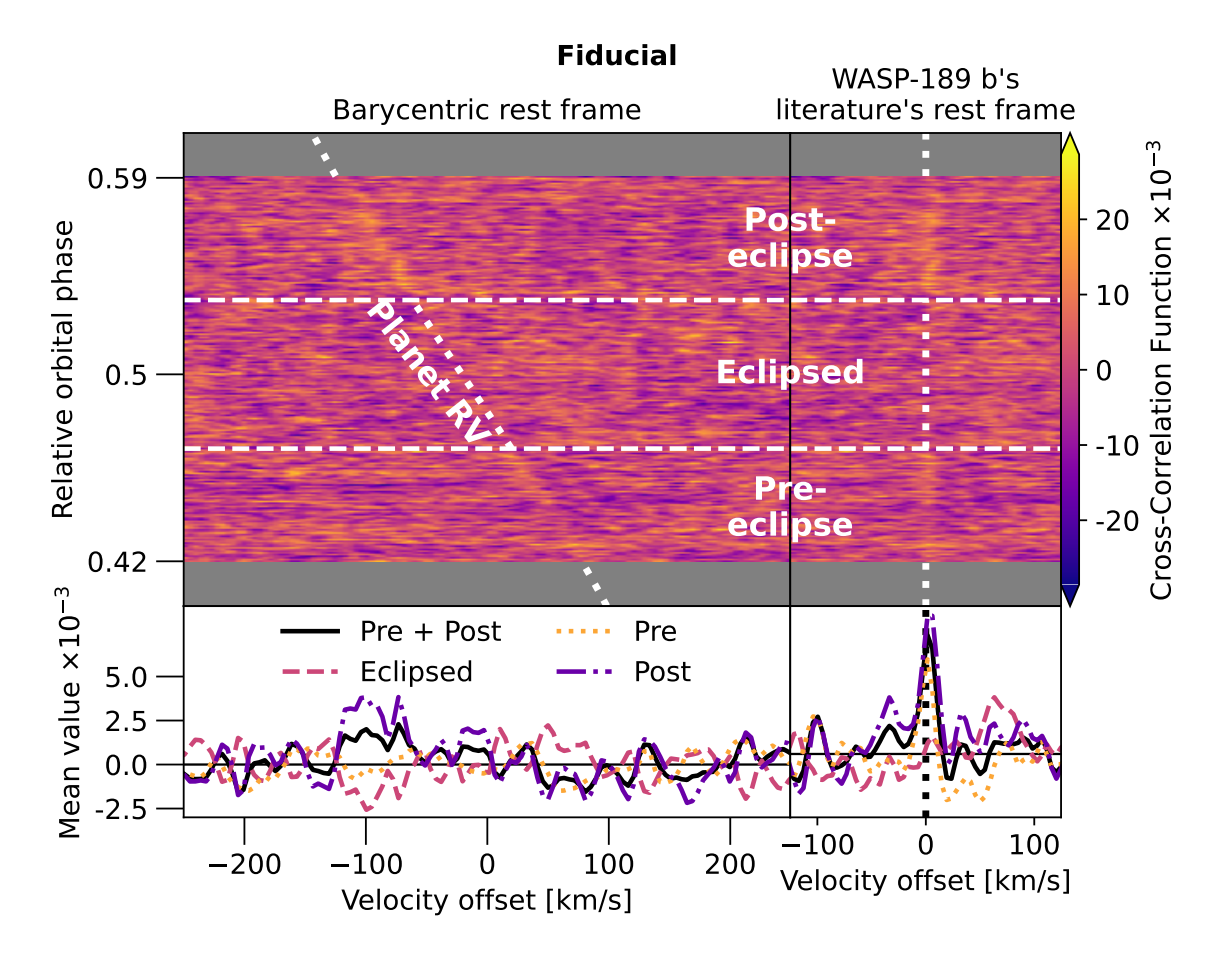


Figure 8. Cross-Correlation Function (CCF) time series for the fiducial spectral template showing the exoplanet's Doppler signature is visible on both nights. Top rows: CCF-value in the barycentric rest frame (left) or WASP-189 b's a literature's rest frame (right; assuming the literature values of  $K_p$  and  $v_{sys}$  listed in Table 1). The planet's expected radial velocity trail (RV) is drawn as a white dotted line. Pre-eclipse, post-eclipse, and eclipsed phases are indicated. Bottom rows: Mean values of the CCF in each rest frame for a subset of orbital phases as shown in the legend.

wavelength range, namely from the optical to the near-infrared.

# 6.2. Titanium chemistry

We notably do not detect Ti<sup>+</sup>, Ti, or TiO in the emission spectrum of WASP-189 b. These results are consistent with results from GHOST by Deibert et al. (2024) who did not detect titanium-bearing species in the optical emission spectra of WASP-189 b. In contrast, ionized titanium, titanium, and titanium oxide have all been detected in the terminator regions of WASP-189 b using transmission spectroscopy (Prinoth et al. 2022, 2023, 2024).

Our injection-recovery tests demonstrate we are not sufficiently sensitive to the titanium oxide and ionized titanium at the chemical abundances from equilibrium chemistry. For TiO, this is attributed to the expected low chemical abundance (  $logX_{\rm TiO} < -7$  at any pressure). For ionized titanium, there are not enough sufficiently strong lines in the J-band to be detectable. In

contrast, our injection-recovery test recovers the neutral titanium spectral template at equilibrium chemical abundances at a S/N=5.8. However, this is less than half of the retrieved injection iron-only model S/N=13.8. Given that for iron, our observed S/N is about half of the injected S/N, we speculate the observed S/N for titanium to be too low to be detectable.

Despite this, if we assume the non-detection of neutral titanium on the dayside is significant, we discuss four explanations: (1) cold-trapping, (2) increased ionization of titanium, (3) line list inaccuracies, and (4) masking of the titanium lines below the H<sup>-</sup> continuum.

In the case of cold-trapping, titanium-bearing species condense on the night side, sinking to deeper parts of the atmosphere that are not probed by emission HRS (Parmentier et al. 2013). This mechanism is disfavored in the case of WASP-189 b for two reasons. First, it would require a circulation pattern with effective vertical mixing around the terminator regions, but without transport to the dayside. Second, for WASP-189 b, the

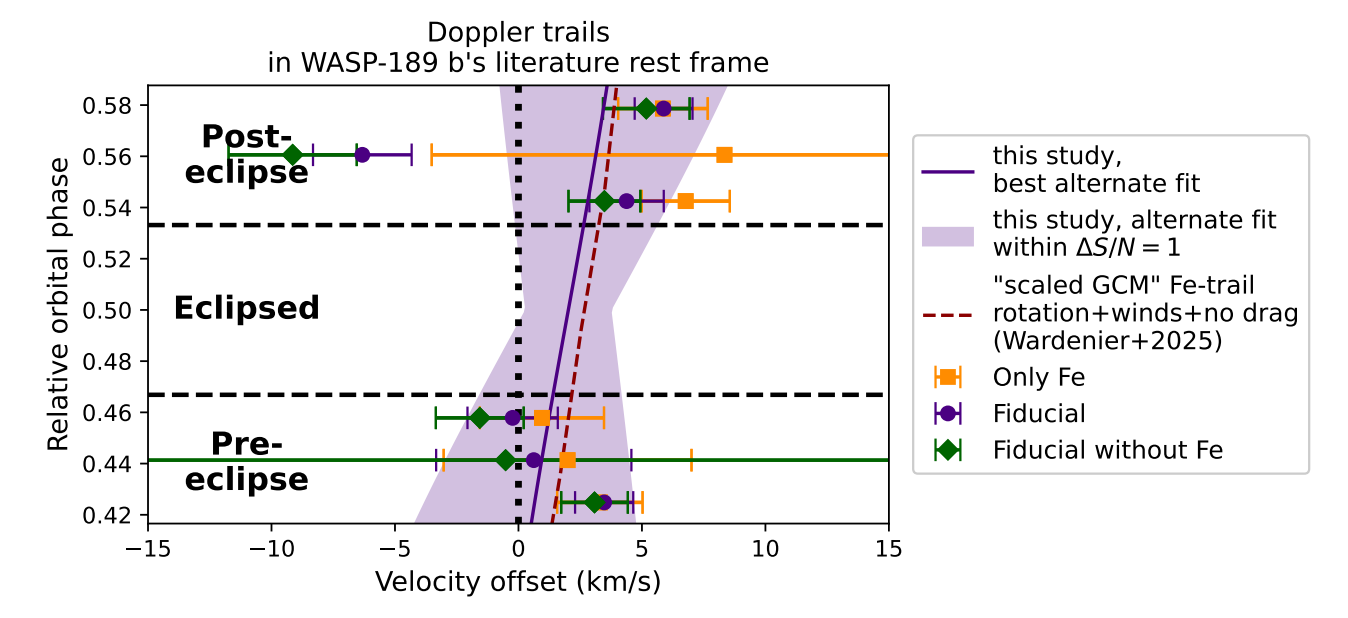


Figure 9. The scatter points mark the velocity offsets resulting from a Gaussian fit to the binned CCF time series in WASP-189 b's literature rest frame ( $v_{\rm sys}$  and  $K_{\rm p}$  listed in Table 1). Three bins are used pre-eclipse and post-eclipse. The scatter points' colors correspond to different spectral templates: only-iron (at equilibrium chemical abundance), fiducial without titanium (our highest S/N template) and fiducial without iron and titanium. The purple line indicates our best alternative orbital fit compared to the literature, for the highest S/N spectral template, where the purple shaded region indicates orbital fits consistent within  $\Delta S/N = S/N_{\rm peak} - S/N_{\rm velocity}$  offset = 1. This is compared against predictions by a GCM (red dashed line) for the velocity offset of iron lines in another typical UHJ, but with the slope scaled to the rotational velocity of WASP-189 b. This GCM model included the effect of rotation, winds, and assumed no drag. Our alternative orbital fit is consistent with the literature, and its additional slope is consistent with 3D effects.

nightside is possibly too hot for cold-trapping; Deline et al. (2022) set a 2250 K upper limit on the nightside temperature, constrained by degeneracies between the geometric albedo and the heat redistribution efficiency. This is above the condensation temperature of neutral titanium (Pelletier et al. 2023) at the higher end.

Another explanation may be that the ionization of titanium is more efficient than expected from equilibrium chemistry, and all the dayside titanium is in an ionized form. To deplete titanium by one order of magnitude, we find that equilibrium chemistry models require an atmosphere that is  $\sim 500$  K hotter than constrained by Yan et al. (2020) at the pressures where the line cores form. Yan et al. (2020) tightly constrained the upper atmospheric temperature to  $T_{\rm upper} = 4340^{+120}_{-100} {\rm K}$  at pressures below  $\log P_{\rm upper} = -3.10^{+0.23}_{-0.25}$ . However, this maximum temperature is set by the conditions in the region where the neutral iron line cores form ( $\sim 0.1 - 1 \text{ mbar}$ ), where NLTE such as photo-ionization are expected to be negligible. Their observations lack sensitivity at significantly lower pressures, where NUV transmission spectroscopy observations by CUTE have constrained much hotter temperatures ( $\sim 15,000$  K, see Sreejith et al. 2023). In any case, we tested this by computing an additional fiducial spectral template using the CUTE

constraints on the thermal profile of WASP-189 b (see Fig. 10) and using FASTCHEM to compute the chemical profiles. Compared to the P-T profile by Yan et al. (2022), the CUTE P-T profile is slightly hotter and has a monotonically increasing hotter upper atmosphere. A cross-correlation analysis detects this spectral template at a slightly higher S/N = 9.9, which is slightly higher, but approximately similar to the fiducial model by Yan et al. (2020) which was detected at a S/N = 9.8. This comparable S/N may be explained by the similarity of the P-T profiles around the pressures where the iron line cores form ( $\sim 0.1$  mbar, see Fig. 10). This result indicates that an overall slightly hotter atmosphere, particularly where the continuum forms, is also consistent with the WINERED data; possibly explaining increased titanium depletion. Regardless, ionized titanium was undetected, even using our high chemical abundance spectral template (see Fig. 16). Injection-recovery only tentatively detected this spectral template at S/N = 3.9. This demonstrates that the WINERED data is not sufficiently sensitive to Ti<sup>+</sup>.

Third, the line lists for the titanium-bearing species may not be sufficiently accurate (Hoeijmakers et al. 2015). We aimed to use the most up-to-date line list of TiO, Ti, and Ti<sup>+</sup> available. However, Prinoth et al.

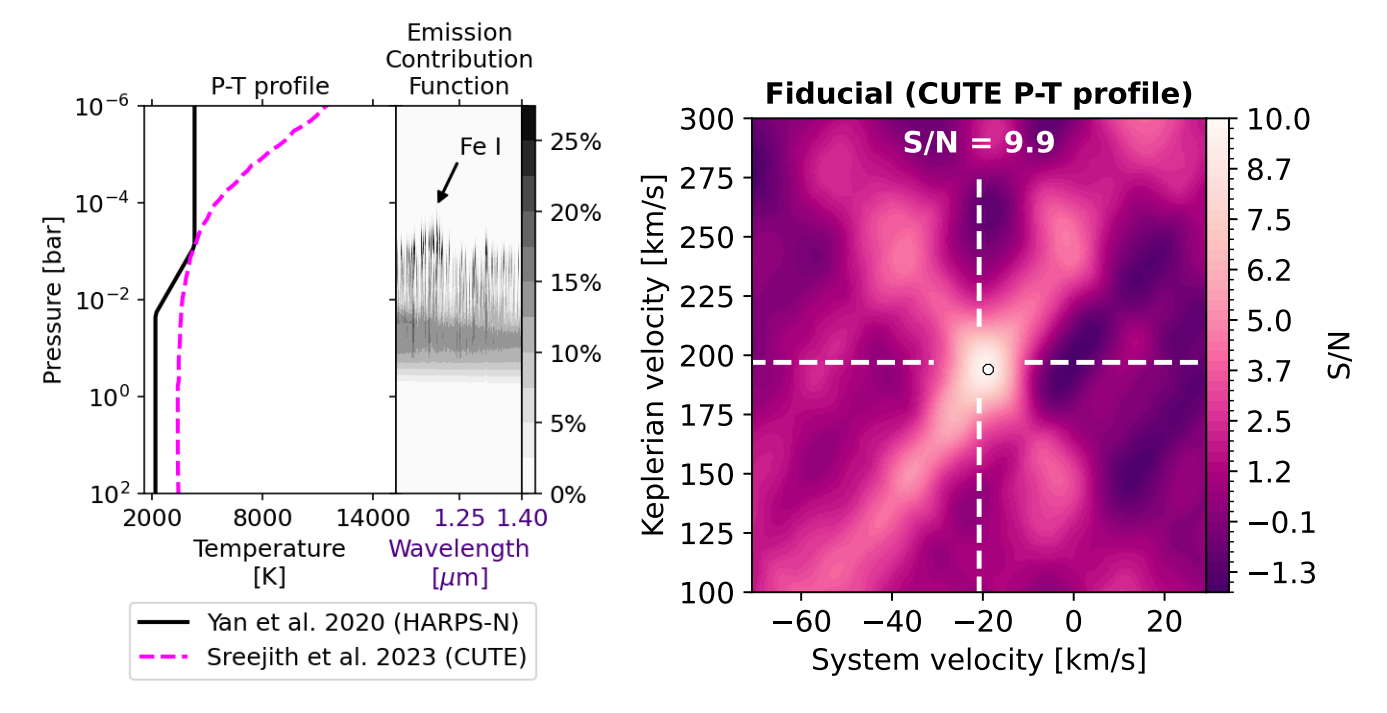


Figure 10. Left: the left panel shows a comparison between the P-T profile from Yan et al. (2020) who used HARPS-N emission spectroscopy and the the P-T profile constrained by Sreejith et al. (2023) who used CUTE NUV transit observations. The right panel shows the Emission Contribution Function for the fiducial spectral template using the CUTE P-T profile. A strong neutral iron emission line core is indicated. Right: similar to the S/N maps of Fig. 6, but shown for the fiducial spectral template that uses the P-T profile from CUTE and with chemical profiles computed using FASTCHEM. This spectral template is detected at a S/N = 9.9.

(2024) excluded certain wavelength parts of their analysis, due to known inaccuracies in their Ti line list, albeit in the optical regime. Serindag et al. (2021) found that using different TiO line lists can impact previously reported detection significances in the atmosphere of the UHJ WASP-33 b.

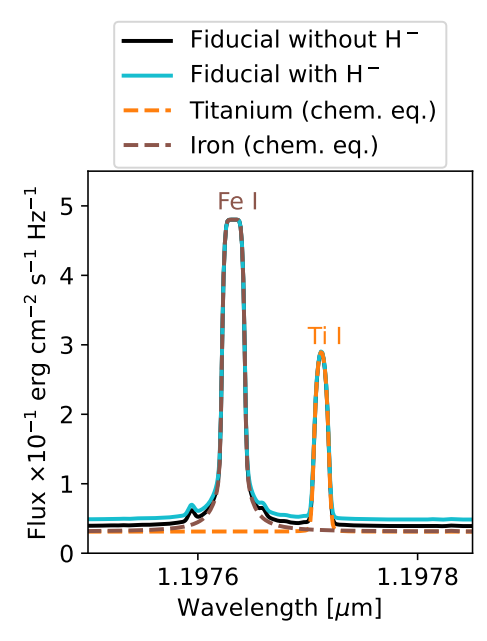
Fourth, H<sup>-</sup> opacity may effectively obscure emission lines, particularly those forming at deeper pressures than iron lines. Since our original model did not include H<sup>-</sup> opacity, we tested its effect by creating a spectral template that incorporated H<sup>-</sup> using PETITRADTRANS, which implements the effects of H<sup>-</sup> following Gray (2008). Indeed, we find that the H<sup>-</sup>-continuum mutes all spectral features, including both iron and titanium lines, and the effect is relatively stronger for the lines forming at deeper pressures. However, the effect is negligible relative to our spectral features (see Fig. 11), and unsurprisingly, cross-correlation with the fiducial spectral template with H<sup>-</sup> indicates a non-significant change in the S/N ratio as the S/N = 9.7, comparable to the S/N of the fiducial spectral template.

### 6.3. Other atmospheric species

The significant detection (S/N = 7.2) of the fiducial spectral template without iron suggests the combined set of Mg, Si, Cr, Al, Na, V, Ca, K, VO, FeH,

and TiO is detected. Silicon, magnesium, chromium, and aluminum all show a peak S/N close to the measured  $v_{\rm sys}$  and  $K_{\rm p}$  values. These four sources also show the most significant drop in S/N when removed from the fiducial model (see Fig. 7). Alongside this, spectral templates with silicon (both chemical equilibrium and higher chemical abundance) and magnesium (at higher chemical abundance) were tentatively detected, e.g., S/N > 4. Altogether, these results hint towards tentative signals of silicon, magnesium, chromium, and aluminum in the WINERED data, but are not conclusive from these data alone.

The non-detection of other atmospheric species than neutral iron is consistent with previous findings in the optical and near-infrared. Yan et al. (2020) also searched for Fe<sup>+</sup>, Ti, Ti<sup>+</sup>, TiO, and VO, and Deibert et al. (2024) checked for all species included in this work. Both studies resulted in null detections of anything other than iron. However, for Ti<sup>+</sup>, Deibert et al. (2024) used a binary mask instead of a spectral template, and this null detection may be attributed to this. Similar to our study, the fiducial model from Deibert et al. (2024) was detected at a higher S/N-ratio than neutral iron alone (S/N = 7.8) instead of S/N = 5.5, indicating the presence of a set of trace species.



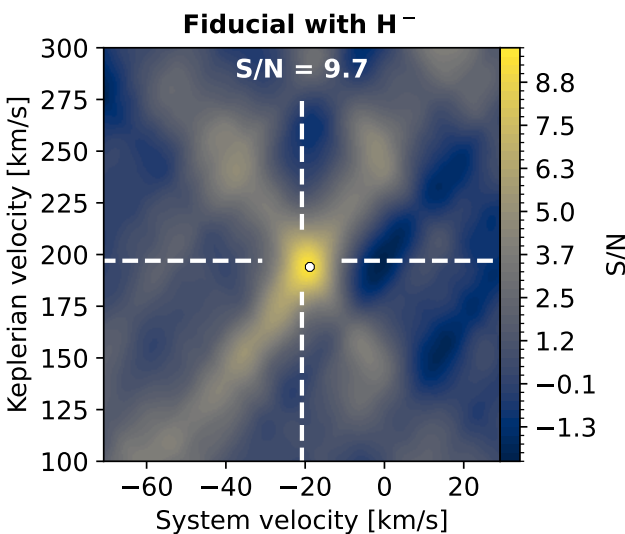


Figure 11. Top: zoom of the fiducial spectral template with and without H<sup>-</sup> around 1.1977  $\mu$ m showing a titanium and iron emission line. The effect on both lines is negligible. Bottom: similar to Fig. 6, but for the fiducial spectral template with H<sup>-</sup> opacity included, which is detected at a comparable S/N = 9.7.

## 6.4. Hints of 3D effects

Our  $K_{\rm p}=194^{+7}_{-6}$  km/s value is consistent with the literature value of  $K_{\rm p}=197^{+15}_{-16}$  km/s computed from the radial velocity signature measured by Anderson et al. (2018) assuming a circular orbit. However, our slightly lower  $K_{\rm p}$ -value could also be hinting towards 3D effects. Zhang et al. (2017) predicted that HJ rotation and winds can result in 1-3 km/s net Doppler offsets. Beltz et al. (2022) showed this can result in orbital phase-dependent

Doppler shifts of similar magnitude using emission HRS. Hoeijmakers et al. (2024) have pointed out that for a synchronized rotation rate, the measured Keplerian velocity would be lower than the expected velocity due to what parts of the exoplanet's disk are visible. Wardenier et al. (2025) generalize this towards  $|\Delta K_{\rm p}| < v_{\rm rot} + v_{\rm jet}$ . This results in a slope of our alternate orbital fit when plotted in the literature's planet's rest frame as shown in Fig. 9. We also over-plot the Doppler shift based on a modified GCM prediction for another UHJ WASP-76 b for iron lines by Wardenier et al. (2025). This was done by taking the Doppler trail for iron as a function of the orbital phase for the drag-free GCM with Doppler shifts from rotation and winds included, and scaling the slope according to the rotational velocity ratio between WASP-189 b and WASP-76 b (assuming a synchronized orbit). The 'scaled GCM' iron Doppler trail is a close match to our alternate orbital fit. We do not find significant evidence for a shift between Doppler trails for the three spectral templates.

Our results from the Doppler shifts are consistent with the Doppler broadening we measured of  $\delta v_{\rm broad} = 6.2 \pm 0.9$  km/s for the fiducial model,  $\delta v_{\rm broad} = 5.4 \pm 0.2$  km/s for the iron-only model, and  $\delta v_{\rm broad} = 6.9 \pm 0.8$  km/s for the fiducial model without iron. This is in line with values derived by Lesjak et al. (2025) who measured day-to-night side winds of  $4.4^{+1.8}_{-1.2}$  km/s and an additional eastward jet of  $1.0^{+0.9}_{-1.8}$  km/s. The measurement of significant rotational broadening, but absence of a strong offset in  $\Delta v_{\rm sys}$  is consistent with results by Beltz et al. (2021), who found cross-correlation with a 3D GCM spectral template with and without Doppler effects, mainly increases the broadening in the S/N-map, but did not result in additional the velocity offset.

# 7. CONCLUSIONS

In this work, we presented the analysis of two nights of HRS data of the UHJ WASP-189 b, obtained with the recently deployed WINERED spectrograph at the 6.5 m Clay/Magellan II Telescope located at Las Campanas Observatory in Chile. The results establish WINERED as an exoplanet atmosphere characterization instrument in the J-band, bridging the optical and near-infrared regimes. The main conclusions of this work are:

1. The atmosphere of WASP-189 b is detected with WINERED/HIRES-J at a high  $S/N \sim 10$ . Previously constrained thermal profiles derived from NIR emission spectroscopy from Yan et al. (2020) (S/N=9.8), as well as a slightly hotter thermal profile inferred from NUV transit observations from Sreejith et al. (2023) (S/N=9.9), both provide a good match to our data.

- 2. We detect neutral iron emission lines in the atmosphere of WASP-189 b at a S/N=6.3, indicating an inversion layer. This result is consistent with previous HRS reconnaissance of this planet using different instruments and wavelength bands.
- 3. We detect the fiducial model without iron at a S/N=7.2. This suggests a combined set of trace species, despite not being detectable individually. Comparison with models that excluded one opacity source from our fiducial model hints that this can be mostly attributed to neutral magnesium (Mg), chromium (Cr), aluminum (Al), and silicon (Si). Individually, neutral silicon is tentatively detected in the WINERED data at a S/N=4.1, assuming chemical equilibrium, and neutral magnesium at a S/N=4.3, assuming an enhanced chemical abundance compared to equilibrium chemistry ( $\log VMR=-4$ ).

### Subsidiary conclusions are:

- 3. Using WINERED with AB nodding, we observed a more stable continuum S/N between consecutive frames compared to ABBA nodding. This can likely be attributed to the mitigation of detector persistence, flat field systematics, or pointing errors while guiding on target.
- 4. The disappearance of the Doppler trail during the secondary eclipse highlights the benefits of observing (part) of the secondary eclipse, to unambiguously confirm that the signal originates from the planet and cannot be attributed to correlated noise, telluric correction, or the stellar lines.
- 5. The measured phase-dependent velocity shifts and velocity broadening are consistent with a 3D circulation where WASP-189 b has a synchronous rotation rate with an additional atmospheric jet.

Finally, we highlight some directions for future research. First, more observations or combining these observations with existing data sets would help to confirm the trace species individually, particularly to verify the tentative detections of silicon and magnesium. Second, this study adds to the emerging evidence that iron can be observed over a wide wavelength range from the optical to the near-infrared. This implies a range of weak and strong spectral lines probing different atmospheric layers and depths. A study combining all of these data will provide high sensitivity to the P-T structure, possibly winds at different atmospheric layers (e.g. Kesseli

et al. 2024) and trace wavelength-dependent differences in where the spectral continuum forms. Third, multiple nights on an optical spectrograph would be better suited to test the hypothesis of ionized titanium on the dayside of UHJs like WASP-189 b. Finally, our injection-recovery tests show WINERED should be highly sensitive to TiO, FeH, and VO at higher chemical abundances. Targeting hot Jupiters with a cooler dayside, but sufficiently hot nightside to prevent cold-trapping, will increase the likelihood of detecting these molecules with WINERED.

Facilities: LCO(WINERED)

Software: The software accompanying this work is available on the first author's GitHub<sup>6</sup> and archived in Zenodo (van Sluijs 2025), Astropy (Astropy Collaboration et al. 2013, 2018, 2022), Matplotlib (Hunter 2007), PETITRADTRANS (Mollière et al. 2019), WARP (Hamano et al. 2024), FASTCHEM (Stock et al. 2018), Numpy (Harris et al. 2020), Scipy (Virtanen et al. 2020), POSEIDON (MacDonald & Madhusudhan 2017; MacDonald 2023)

We would like to thank the anonymous reviewer for their insightful comments which have improved the quality of this work. We would like to thank Sam de Regt for providing the latest hyVO line list in a format suit-vate communication, which improved the quality of this work. This paper is based on WINERED data gathered with the 6.5 m Clay/Magellan II Telescope located at Las Campanas Observatory, Chile. WINERED was developed by the University of Tokyo and the Laboratory of Infrared High-resolution Spectroscopy, Kyoto Sangyo University, under the financial support of KAKENHI (Nos. 16684001, 20340042, 21840052, and 26287028) and the MEXT Supported Program for the Strategic Research Foundation at Private Universities (Nos. S0801061 and S1411028). The observing runs in 2023 June and 2024 April were partly supported by KAKENHI (grant No. 19KK0080) and JSPS Bilateral Program Number JPJSBP120239909. This work also received financial support from the Heising-Simons Foundation, Grant #2019-1403. A portion of this research was carried out at the Jet Propulsion Laboratory, California Institute of Technology, under a contract with the National Aeronautics and Space Administration (80NM0018D0004).

### REFERENCES

- Ahrer, E.-M., Alderson, L., & Bean, J. L. e. a. 2023, The Astrophysical Journal Letters, 936, L19, doi: 10.3847/2041-8213/ac8c48
- Anderson, D. R., Temple, L. Y., Nielsen, L. D., et al. 2018, arXiv e-prints, arXiv:1809.04897, doi: 10.48550/arXiv.1809.04897
- Arcangeli, J., Désert, J.-M., Line, M. R., et al. 2018, The Astrophysical Journal Letters, 855, L30, doi: 10.3847/2041-8213/aab272
- Asplund, M., Grevesse, N., Sauval, A. J., & Scott, P. 2009, ARA&A, 47, 481,
  - doi: 10.1146/annurev.astro.46.060407.145222
- Astropy Collaboration, Robitaille, T. P., Tollerud, E. J., et al. 2013, A&A, 558, A33, doi: 10.1051/0004-6361/201322068
- Astropy Collaboration, Price-Whelan, A. M., Sipőcz, B. M., et al. 2018, AJ, 156, 123, doi: 10.3847/1538-3881/aabc4f
- Astropy Collaboration, Price-Whelan, A. M., Lim, P. L., et al. 2022, ApJ, 935, 167, doi: 10.3847/1538-4357/ac7c74
- Azevedo Silva, T., Demangeon, O. D. S., Santos, N. C., et al. 2022, A&A, 666, L10, doi: 10.1051/0004-6361/202244489
- Barman, T. S., Hauschildt, P. H., Schweitzer, A., et al. 2002, ApJL, 569, L51, doi: 10.1086/340579
- Bello-Arufe, A., Cabot, S. H. C., Mendonça, J. M.,
  Buchhave, L. A., & Rathcke, A. D. 2022, AJ, 163, 96,
  doi: 10.3847/1538-3881/ac402e
- Beltz, H., & Rauscher, E. 2024, arXiv e-prints, arXiv:2409.13840, doi: 10.48550/arXiv.2409.13840
- Beltz, H., Rauscher, E., Brogi, M., & Kempton, E. M. R. 2021, AJ, 161, 1, doi: 10.3847/1538-3881/abb67b
- Beltz, H., Rauscher, E., Kempton, E. M. R., et al. 2022, AJ, 164, 140, doi: 10.3847/1538-3881/ac897b
- Beltz, H., Rauscher, E., Kempton, E. M. R., Malsky, I., & Savel, A. B. 2023, AJ, 165, 257, doi: 10.3847/1538-3881/acd24d
- Birkby, J. L., de Kok, R. J., Brogi, M., et al. 2013, MNRAS, 436, L35, doi: 10.1093/mnrasl/slt107
- Borsa, F., Fossati, L., Koskinen, T., Young, M. E., & Shulyak, D. 2021, Nature Astronomy, 6, 226, doi: 10.1038/s41550-021-01544-4
- Borsato, N. W., Hoeijmakers, H. J., Prinoth, B., et al. 2023, A&A, 673, A158, doi: 10.1051/0004-6361/202245121
- Borysow, A. 2002, A&A, 390, 779, doi: 10.1051/0004-6361:20020555
  - <sup>6</sup> https://github.com/lennartvansluijs/WINERED-WASP-189-b

- Borysow, A., & Frommhold, L. 1989, ApJ, 341, 549, doi: 10.1086/167515
- Borysow, A., Frommhold, L., & Moraldi, M. 1989, ApJ, 336, 495, doi: 10.1086/167027
- Borysow, A., Jorgensen, U. G., & Fu, Y. 2001, JQSRT, 68, 235, doi: 10.1016/S0022-4073(00)00023-6
- Borysow, J., Frommhold, L., & Birnbaum, G. 1988, ApJ, 326, 509, doi: 10.1086/166112
- Bowesman, C. A., Qu, Q., McKemmish, L. K., Yurchenko, S. N., & Tennyson, J. 2024, MNRAS, 529, 1321, doi: 10.1093/mnras/stae542
- Brogi, M., de Kok, R. J., Albrecht, S., et al. 2016, ApJ, 817, 106, doi: 10.3847/0004-637X/817/2/106
- Brogi, M., & Line, M. R. 2019, AJ, 157, 114, doi: 10.3847/1538-3881/aaffd3
- Brogi, M., Snellen, I. A. G., de Kok, R. J., et al. 2012, Nature, 486, 502, doi: 10.1038/nature11161
- Brogi, M., Emeka-Okafor, V., Line, M. R., et al. 2022, arXiv e-prints, arXiv:2209.15548. https://arxiv.org/abs/2209.15548
- Cabot, S. H. C., Madhusudhan, N., Welbanks, L., Piette, A., & Gandhi, S. 2020, MNRAS, 494, 363, doi: 10.1093/mnras/staa748
- Casasayas-Barris, N., Pallé, E., Yan, F., et al. 2019, A&A, 628, A9, doi: 10.1051/0004-6361/201935623
- Cont, D., Yan, F., Reiners, A., et al. 2022, A&A, 668, A53, doi: 10.1051/0004-6361/202244277
- Coulombe, L.-P., Benneke, B., Challener, R., et al. 2023, Nature, 620, 292, doi: 10.1038/s41586-023-06230-1
- Deibert, E. K., Langeveld, A. B., Young, M. E., et al. 2024, AJ, 168, 148, doi: 10.3847/1538-3881/ad643f
- Deline, A., Hooton, M. J., Lendl, M., et al. 2022, A&A, 659, A74, doi: 10.1051/0004-6361/202142400
- Deming, D., Wilkins, A., & McCullough, P. e. a. 2013, The Astrophysical Journal, 774, 95, doi: 10.1088/0004-637X/774/2/95
- Evans, T. M., Pontoppidan, K. M., & Rustamkulov, Z. e. a. 2023, The Astrophysical Journal Letters, 939, L31, doi: 10.3847/2041-8213/ac9ad1
- Evans, T. M., Sing, D. K., Wakeford, H. R., et al. 2016, ApJL, 822, L4, doi: 10.3847/2041-8205/822/1/L4
- Feinstein, A. D., Kammer, J. A., & Fortney, J. J. e. a. 2023, Nature, 620, 227–231, doi: 10.1038/s41586-023-05848-z
- Fortney, J. J., Dawson, R. I., & Komacek, T. D. 2021, Journal of Geophysical Research (Planets), 126, e06629, doi: 10.1029/2020JE006629
- Fortney, J. J., Lodders, K., Marley, M. S., & Freedman,R. S. 2008, ApJ, 678, 1419, doi: 10.1086/528370

- Fossati, L., Koskinen, T., Lothringer, J. D., et al. 2018, ApJL, 868, L30, doi: 10.3847/2041-8213/aaf0a5
- Fossati, L., Young, M. E., Shulyak, D., et al. 2021, A&A, 653, A52, doi: 10.1051/0004-6361/202140813
- Gandhi, S., Kesseli, A., Snellen, I., et al. 2022, MNRAS, 515, 749, doi: 10.1093/mnras/stac1744
- Gandhi, S., Landman, R., Snellen, I., et al. 2024, MNRAS, 530, 2885, doi: 10.1093/mnras/stae1048
- Gandhi, S., Kesseli, A., Zhang, Y., et al. 2023, AJ, 165, 242, doi: 10.3847/1538-3881/accd65
- Giacobbe, P., Brogi, M., Gandhi, S., et al. 2021, Nature, 592, 205, doi: 10.1038/s41586-021-03381-x
- Gibson, N. P., Merritt, S., Nugroho, S. K., et al. 2020, MNRAS, 493, 2215, doi: 10.1093/mnras/staa228
- Gray, D. F. 2008, The Observation and Analysis of Stellar Photospheres
- Guo, B., Yan, F., Nortmann, L., et al. 2024, A&A, 687, A103, doi: 10.1051/0004-6361/202449890
- Hamano, S., Ikeda, Y., Otsubo, S., et al. 2024, PASP, 136, 014504, doi: 10.1088/1538-3873/ad1b38
- Harris, C. R., Millman, K. J., van der Walt, S. J., et al. 2020, Nature, 585, 357, doi: 10.1038/s41586-020-2649-2
- Herman, M. K., de Mooij, E. J. W., Nugroho, S. K., Gibson, N. P., & Jayawardhana, R. 2022, arXiv e-prints, arXiv:2203.11188. https://arxiv.org/abs/2203.11188
- Hoeijmakers, H. J., de Kok, R. J., Snellen, I. A. G., et al. 2015, A&A, 575, A20, doi: 10.1051/0004-6361/201424794
- Hoeijmakers, H. J., Ehrenreich, D., Heng, K., et al. 2018, Nature, 560, 453, doi: 10.1038/s41586-018-0401-y
- Hoeijmakers, H. J., Seidel, J. V., Pino, L., et al. 2020, A&A, 641, A123, doi: 10.1051/0004-6361/202038365
- Hoeijmakers, H. J., Kitzmann, D., Morris, B. M., et al. 2022, arXiv e-prints, arXiv:2210.12847, doi: 10.48550/arXiv.2210.12847
- —. 2024, A&A, 685, A139,doi: 10.1051/0004-6361/202244968
- Hubeny, I., Burrows, A., & Sudarsky, D. 2003, ApJ, 594, 1011, doi: 10.1086/377080
- Huitson, C. M., Sing, D. K., Vidal-Madjar, A., et al. 2012, Monthly Notices of the Royal Astronomical Society, 422, 2477, doi: 10.1111/j.1365-2966.2012.20811.x
- Hunter, J. D. 2007, Computing in Science & Engineering, 9, 90, doi: 10.1109/MCSE.2007.55
- Ikeda, Y., Kondo, S., Otsubo, S., et al. 2022, PASP, 134, 015004, doi: 10.1088/1538-3873/ac1c5f
- Kesseli, A. Y., Beltz, H., Rauscher, E., & Snellen, I. A. G. 2024, arXiv e-prints, arXiv:2409.03124, doi: 10.48550/arXiv.2409.03124
- Kesseli, A. Y., & Snellen, I. A. G. 2021, ApJL, 908, L17, doi: 10.3847/2041-8213/abe047

- Kesseli, A. Y., Snellen, I. A. G., Alonso-Floriano, F. J., Mollière, P., & Serindag, D. B. 2020, AJ, 160, 228, doi: 10.3847/1538-3881/abb59c
- Kesseli, A. Y., Snellen, I. A. G., Casasayas-Barris, N., Mollière, P., & Sánchez-López, A. 2022, AJ, 163, 107, doi: 10.3847/1538-3881/ac4336
- Kondo, S., Ikeda, Y., Kobayashi, N., et al. 2015, arXiv e-prints, arXiv:1501.03403, doi: 10.48550/arXiv.1501.03403
- Kotani, T., Tamura, M., Nishikawa, J., et al. 2018, in Society of Photo-Optical Instrumentation Engineers (SPIE) Conference Series, Vol. 10702, Ground-based and Airborne Instrumentation for Astronomy VII, ed. C. J. Evans, L. Simard, & H. Takami, 1070211, doi: 10.1117/12.2311836
- Landman, R., Sánchez-López, A., Mollière, P., et al. 2021, A&A, 656, A119, doi: 10.1051/0004-6361/202141696
- Lavail, A. 2021, in The 20.5th Cambridge Workshop on Cool Stars, Stellar Systems, and the Sun (CS20.5), Cambridge Workshop on Cool Stars, Stellar Systems, and the Sun, 77, doi: 10.5281/zenodo.4562690
- Lendl, M., Csizmadia, S., Deline, A., et al. 2020, A&A, 643, A94, doi: 10.1051/0004-6361/202038677
- Lesjak, F., Nortmann, L., Cont, D., et al. 2024, arXiv e-prints, arXiv:2411.19662, doi: 10.48550/arXiv.2411.19662
- —. 2025, A&A, 693, A72,doi: 10.1051/0004-6361/202451391
- Levine, S. E., DeGroff, W. T., Bida, T. A., Dunham, E. W., & Jacoby, G. H. 2018, in SPIE Conference Series, Vol. 10700, Ground-based and Airborne Telescopes VII, ed. H. K. Marshall & J. Spyromilio, 107004P, doi: 10.1117/12.2312380
- Lothringer, J. D., Barman, T., & Koskinen, T. 2018, ApJ, 866, 27, doi: 10.3847/1538-4357/aadd9e
- MacDonald, R. J. 2023, The Journal of Open Source Software, 8, 4873, doi: 10.21105/joss.04873
- MacDonald, R. J., & Madhusudhan, N. 2017, MNRAS, 469, 1979, doi: 10.1093/mnras/stx804
- Mansfield, M., Bean, J. L., Line, M. R., et al. 2020, The Astronomical Journal, 160, 5, doi: 10.3847/1538-3881/ab920e
- McCarthy, D. W., Burge, J. H., Angel, J. R. P., et al. 1998, in Society of Photo-Optical Instrumentation Engineers (SPIE) Conference Series, Vol. 3354, Infrared Astronomical Instrumentation, ed. A. M. Fowler, 750–754, doi: 10.1117/12.317340
- McKemmish, L. K., Masseron, T., Hoeijmakers, H. J., et al. 2019, MNRAS, 488, 2836, doi: 10.1093/mnras/stz1818

- McLean, I. S., Becklin, E. E., Bendiksen, O., et al. 1998, in Society of Photo-Optical Instrumentation Engineers (SPIE) Conference Series, Vol. 3354, Infrared Astronomical Instrumentation, ed. A. M. Fowler, 566–578, doi: 10.1117/12.317283
- Merritt, S. R., Gibson, N. P., Nugroho, S. K., et al. 2021, MNRAS, 506, 3853, doi: 10.1093/mnras/stab1878
- Mollière, P., Wardenier, J. P., van Boekel, R., et al. 2019, A&A, 627, A67, doi: 10.1051/0004-6361/201935470
- Moses, J. I., Visscher, C., Fortney, J. J., et al. 2011, The Astrophysical Journal, 737, 15, doi: 10.1088/0004-637X/737/1/15
- Nortmann, L., Lesjak, F., Yan, F., et al. 2024, arXiv e-prints, arXiv:2404.12363, doi: 10.48550/arXiv.2404.12363
- Nugroho, S. K., Gibson, N. P., de Mooij, E. J. W., et al. 2020, MNRAS, 496, 504, doi: 10.1093/mnras/staa1459
- Nugroho, S. K., Kawahara, H., Gibson, N. P., et al. 2021, ApJL, 910, L9, doi: 10.3847/2041-8213/abec71
- Oklopčić, A., & Hirata, C. M. 2018, ApJL, 855, L11, doi: 10.3847/2041-8213/aaada9
- Otsubo, S., Sarugaku, Y., Takeuchi, T., et al. 2024, in Society of Photo-Optical Instrumentation Engineers (SPIE) Conference Series, Vol. 13096, Ground-based and Airborne Instrumentation for Astronomy X, ed. J. J. Bryant, K. Motohara, & J. R. D. Vernet, 1309631, doi: 10.1117/12.3018617
- Ouyang, Q., Wang, W., Zhai, M., et al. 2023, Research in Astronomy and Astrophysics, 23, 065010, doi: 10.1088/1674-4527/accbb2
- Park, C., Jaffe, D. T., Yuk, I.-S., et al. 2014, in SPIE
  Conference Series, Vol. 9147, Ground-based and Airborne
  Instrumentation for Astronomy V, ed. S. K. Ramsay, I. S.
  McLean, & H. Takami, 91471D, doi: 10.1117/12.2056431
- Parmentier, V., Showman, A. P., & Lian, Y. 2013, A&A, 558, A91, doi: 10.1051/0004-6361/201321132
- Parmentier, V., Line, M. R., Bean, J. L., et al. 2018, A&A, 617, A110, doi: 10.1051/0004-6361/201833059
- Pelletier, S., Benneke, B., Ali-Dib, M., et al. 2023, Nature, 619, 491, doi: 10.1038/s41586-023-06134-0
- Petz, S., Johnson, M. C., Asnodkar, A. P., et al. 2025, AJ, 169, 267, doi: 10.3847/1538-3881/adc411
- Petz, S., Johnson, M. C., Pai Asnodkar, A., et al. 2024, arXiv e-prints, arXiv:2407.09643, doi: 10.48550/arXiv.2407.09643
- Pino, L., Désert, J.-M., Brogi, M., et al. 2020, ApJL, 894, L27, doi: 10.3847/2041-8213/ab8c44
- Pino, L., Brogi, M., Désert, J. M., et al. 2022, arXiv e-prints, arXiv:2209.11735. https://arxiv.org/abs/2209.11735

- Piskorz, D., Benneke, B., Crockett, N. R., et al. 2017, AJ, 154, 78, doi: 10.3847/1538-3881/aa7dd8
- Polyansky, O. L., Kyuberis, A. A., Zobov, N. F., et al. 2018, MNRAS, 480, 2597, doi: 10.1093/mnras/sty1877
- Prinoth, B., Hoeijmakers, H. J., Kitzmann, D., et al. 2022, Nature Astronomy, 6, 449, doi: 10.1038/s41550-021-01581-z
- Prinoth, B., Hoeijmakers, H. J., Pelletier, S., et al. 2023, A&A, 678, A182, doi: 10.1051/0004-6361/202347262
- Prinoth, B., Hoeijmakers, H. J., Morris, B. M., et al. 2024, A&A, 685, A60, doi: 10.1051/0004-6361/202349125
- Prinoth, B., Seidel, J. V., Hoeijmakers, H. J., et al. 2025, A&A, 694, A284, doi: 10.1051/0004-6361/202452405
- Quirrenbach, A., Amado, P. J., Caballero, J. A., et al. 2014, in Society of Photo-Optical Instrumentation
  Engineers (SPIE) Conference Series, Vol. 9147,
  Ground-based and Airborne Instrumentation for
  Astronomy V, ed. S. K. Ramsay, I. S. McLean, &
  H. Takami, 91471F, doi: 10.1117/12.2056453
- Rasio, F. A., & Ford, E. B. 1996, Science, 274, 954, doi: 10.1126/science.274.5289.954
- Rayner, J., Tokunaga, A., Jaffe, D., et al. 2016, in SPIE
  Conference Series, Vol. 9908, Ground-based and Airborne
  Instrumentation for Astronomy VI, ed. C. J. Evans,
  L. Simard, & H. Takami, 990884, doi: 10.1117/12.2232064
- Rothman, L. S., Gordon, I. E., Barber, R. J., et al. 2010, JQSRT, 111, 2139, doi: 10.1016/j.jqsrt.2010.05.001
- Scandariato, G., Borsa, F., Bonomo, A. S., et al. 2023, A&A, 674, A58, doi: 10.1051/0004-6361/202245539
- Serindag, D. B., Nugroho, S. K., Mollière, P., et al. 2021, A&A, 645, A90, doi: 10.1051/0004-6361/202039135
- Sheppard, K. B., Mandell, A. M., Tamburo, P., et al. 2017, ApJL, 850, L32, doi: 10.3847/2041-8213/aa9ae9
- Showman, A. P., & Guillot, T. 2002, A&A, 385, 166, doi: 10.1051/0004-6361:20020101
- Simonnin, A., Parmentier, V., Wardenier, J. P., et al. 2024, arXiv e-prints, arXiv:2412.01472, doi: 10.48550/arXiv.2412.01472
- Sing, D. K., Lecavelier des Etangs, A., & Fortney, J. J. e. a. 2013, Monthly Notices of the Royal Astronomical Society, 436, 2956, doi: 10.1093/mnras/stt1782
- Snellen, I. A. G., Brandl, B. R., de Kok, R. J., et al. 2014, Nature, 509, 63, doi: 10.1038/nature13253
- Snellen, I. A. G., de Kok, R. J., de Mooij, E. J. W., & Albrecht, S. 2010, Nature, 465, 1049, doi: 10.1038/nature09111
- Spake, J. J., Sing, D. K., & Wakeford, H. R. e. a. 2021, The Astronomical Journal, 162, 229, doi: 10.3847/1538-3881/ac16e1

- Spring, E. F., Birkby, J. L., Pino, L., et al. 2022, arXiv e-prints, arXiv:2201.03600.
  - https://arxiv.org/abs/2201.03600
- Sreejith, A. G., France, K., Fossati, L., et al. 2023, ApJL, 954, L23, doi: 10.3847/2041-8213/acef1c
- Stangret, M., Casasayas-Barris, N., Pallé, E., et al. 2022, A&A, 662, A101, doi: 10.1051/0004-6361/202141799
- Stock, J. W., Deitloff, L. L. R., Waldmann, D. K., & Geppert, W. R. 2018, Monthly Notices of the Royal Astronomical Society, 479, 865, doi: 10.1093/mnras/sty1659
- Swain, M. R., Deroo, P., Griffith, C. A., et al. 2010, Nature, 463, 637, doi: 10.1038/nature08775
- Thibault, S., Rabou, P., Donati, J.-F., et al. 2012, in SPIE Conference Series, Vol. 8446, Ground-based and Airborne Instrumentation for Astronomy IV, ed. I. S. McLean,
  S. K. Ramsay, & H. Takami, 844630,
  doi: 10.1117/12.926697
- van Sluijs, L. 2025,
  - lennartvansluijs/WINERED-WASP-189-b: WR W189b v1.0, v1.0, Zenodo, doi: 10.5281/zenodo.16113076
- van Sluijs, L., Birkby, J. L., Lothringer, J., et al. 2023, MNRAS, 522, 2145, doi: 10.1093/mnras/stad1103
- Virtanen, P., Gommers, R., Oliphant, T. E., et al. 2020, Nature Methods, 17, 261, doi: 10.1038/s41592-019-0686-2

- Vissapragada, S., McCreery, P., Dos Santos, L. A., et al. 2024, ApJL, 962, L19, doi: 10.3847/2041-8213/ad23cf
- Wardenier, J. P., Parmentier, V., Lee, E. K. H., & Line, M. R. 2025, arXiv e-prints, arXiv:2502.01606, doi: 10.48550/arXiv.2502.01606
- Wardenier, J. P., Parmentier, V., Lee, E. K. H., Line, M. R., & Gharib-Nezhad, E. 2021, MNRAS, 506, 1258, doi: 10.1093/mnras/stab1797
- Wardenier, J. P., Parmentier, V., Line, M. R., & Lee, E. K. H. 2023, MNRAS, 525, 4942, doi: 10.1093/mnras/stad2586
- Wende, S., Reiners, A., Seifahrt, A., & Bernath, P. F. 2010, A&A, 523, A58, doi: 10.1051/0004-6361/201015220
- Wright, S. O. M., Waldmann, I., & Yurchenko, S. N. 2022, MNRAS, 512, 2911, doi: 10.1093/mnras/stac654
- Yan, F., Pallé, E., Reiners, A., et al. 2020, A&A, 640, L5, doi: 10.1051/0004-6361/202038294
- 2022, A&A, 661, L6, doi: 10.1051/0004-6361/202243503
   Young, M. E., Fossati, L., Koskinen, T. T., et al. 2020,
   A&A, 641, A47, doi: 10.1051/0004-6361/202037672
- Young, M. E., Spring, E. F., & Birkby, J. L. 2024, MNRAS, 530, 4356, doi: 10.1093/mnras/stae674
- Yousefi, M., Bernath, P. F., Hodges, J., & Masseron, T. 2018, JQSRT, 217, 416, doi: 10.1016/j.jqsrt.2018.06.016
- Zhang, X., Tian, F., Wang, Y., Dudhia, J., & Chen, M. 2017, ApJL, 837, L27, doi: 10.3847/2041-8213/aa62fc

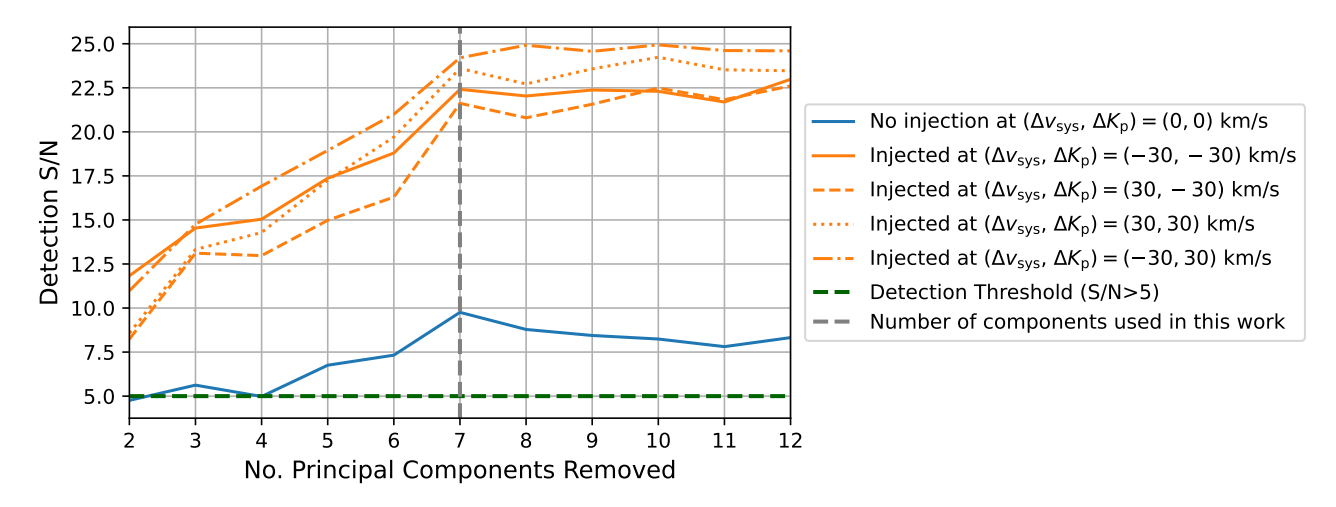


Figure 12. Detection S/N as a function of number of removed principal components. The blue line shows the detection S/N for the observed data without model injection, while the orange lines show the injected data for four different velocity offsets. The dashed green line indicates a detection threshold of S/N > 5.

### **APPENDIX**

### A. ROBUSTNESS OF SVD

To verify the robustness of our main results against various choices of removed components using SVD, we conducted additional injection-recovery tests. We injected our highest S/N model (fiducial without titanium) into the data at a nominal planet-to-star flux ratio at four velocity offsets ( $\Delta v_{\rm sys}$ ,  $\Delta K_{\rm p}$ ). We then calculated the S/N at the injection site, and the results are illustrated in Figure 12. The retrieved S/N increases up to seven components and then levels off, which mirrors the behavior of the actual atmospheric signal when no artificial signal is added. This indicates that using seven components effectively cleans the data while mostly retaining the exoplanet's signal. Furthermore, we found that a wide range of components removed still maintains detection in the real data above a conservative S/N threshold of five. Thus, we argue that the main results of this study are robust against the choice of removed principal components.

### B. ADDITIONAL FIGURES

The next pages contain additional figures to support various parts of this work.

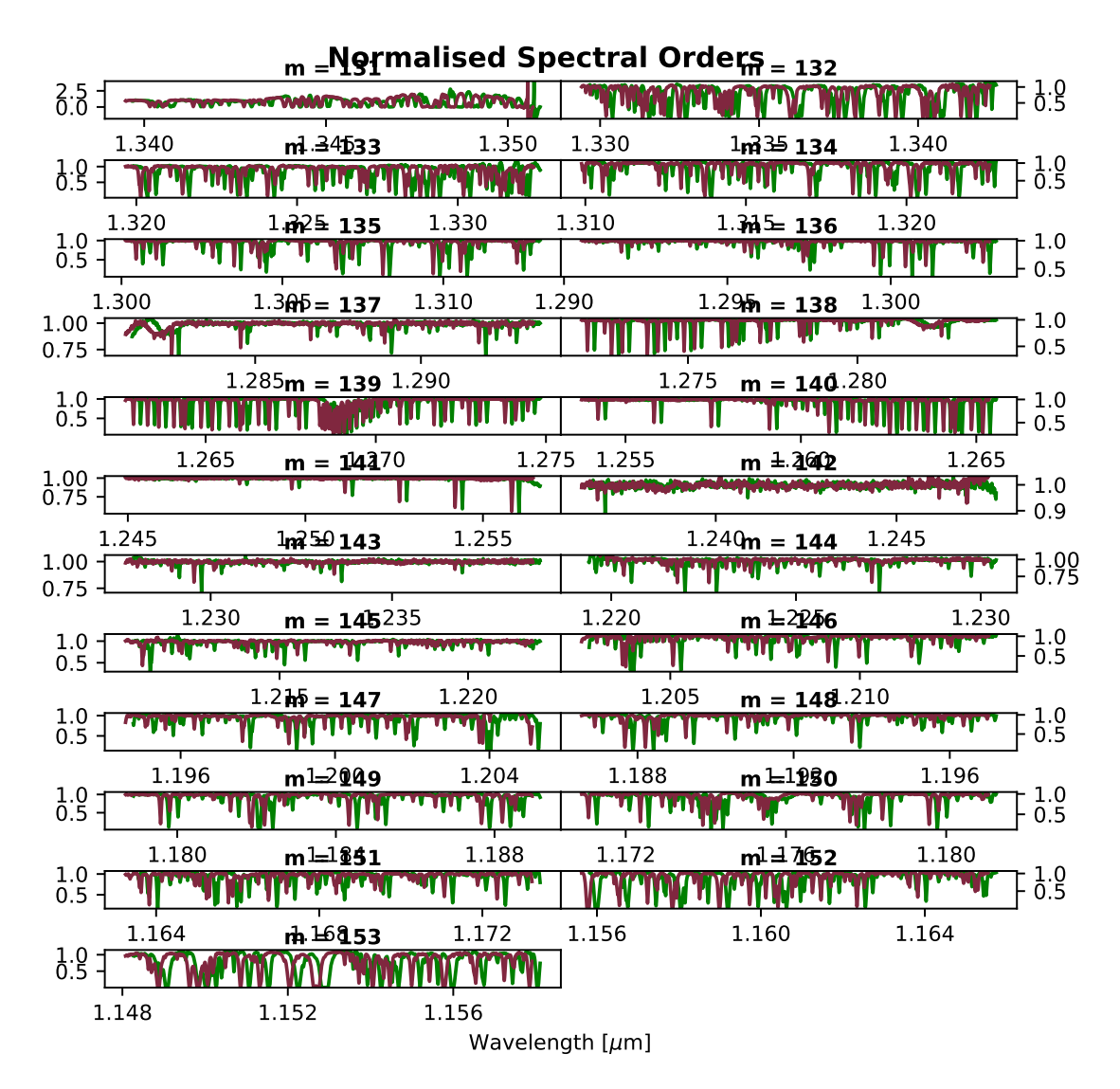


Figure 13. Average obtained normalized spectrum for each spectral order and observing night. The nights have been offset in wavelength for visual purposes. The first night is shown in green and the second night is shown in wine red.

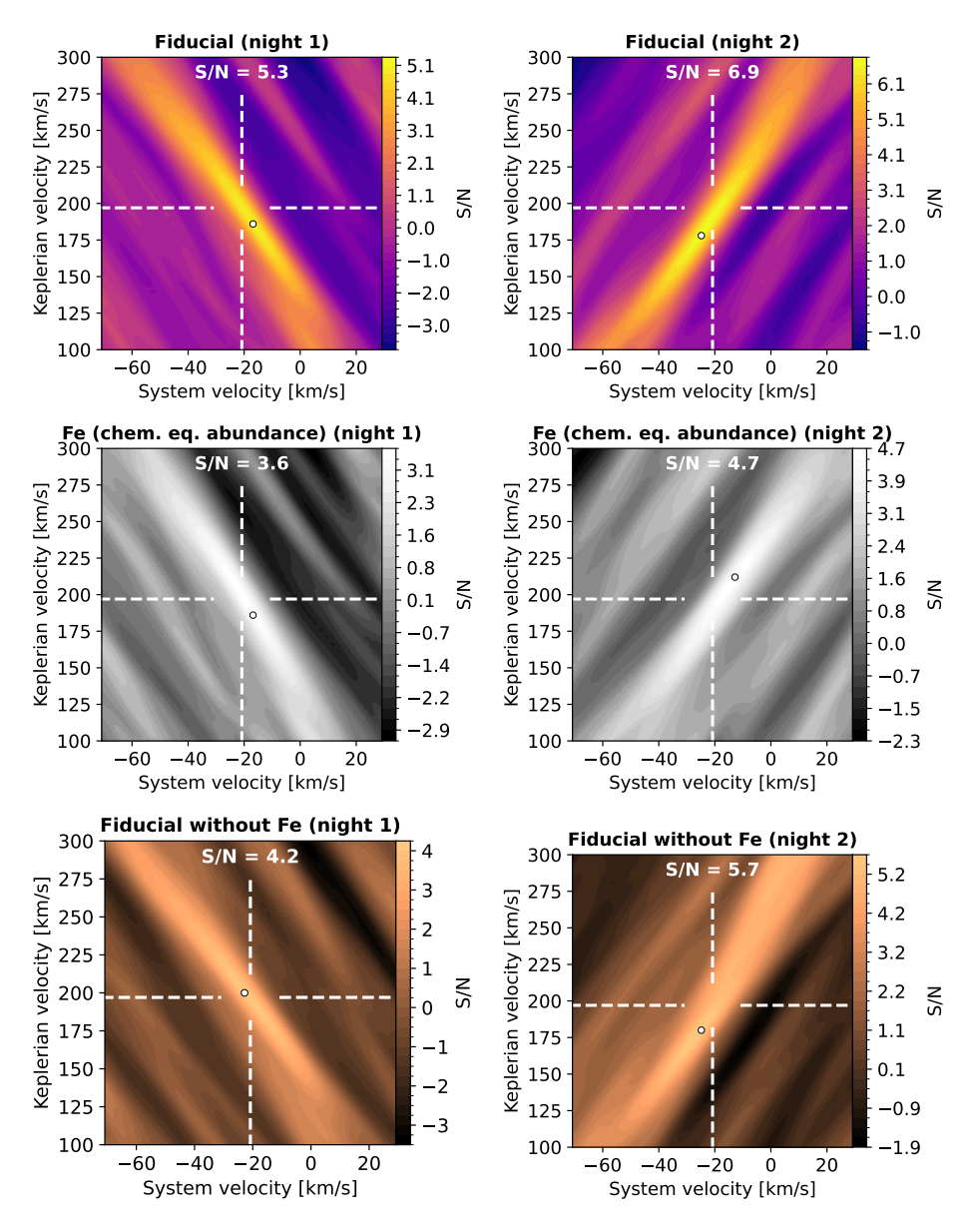


Figure 14. Similar to Fig 6, but instead shown for each night: for the fiducial case, neutral iron (assuming equilibrium chemical abundances), and the fiducial model without iron.

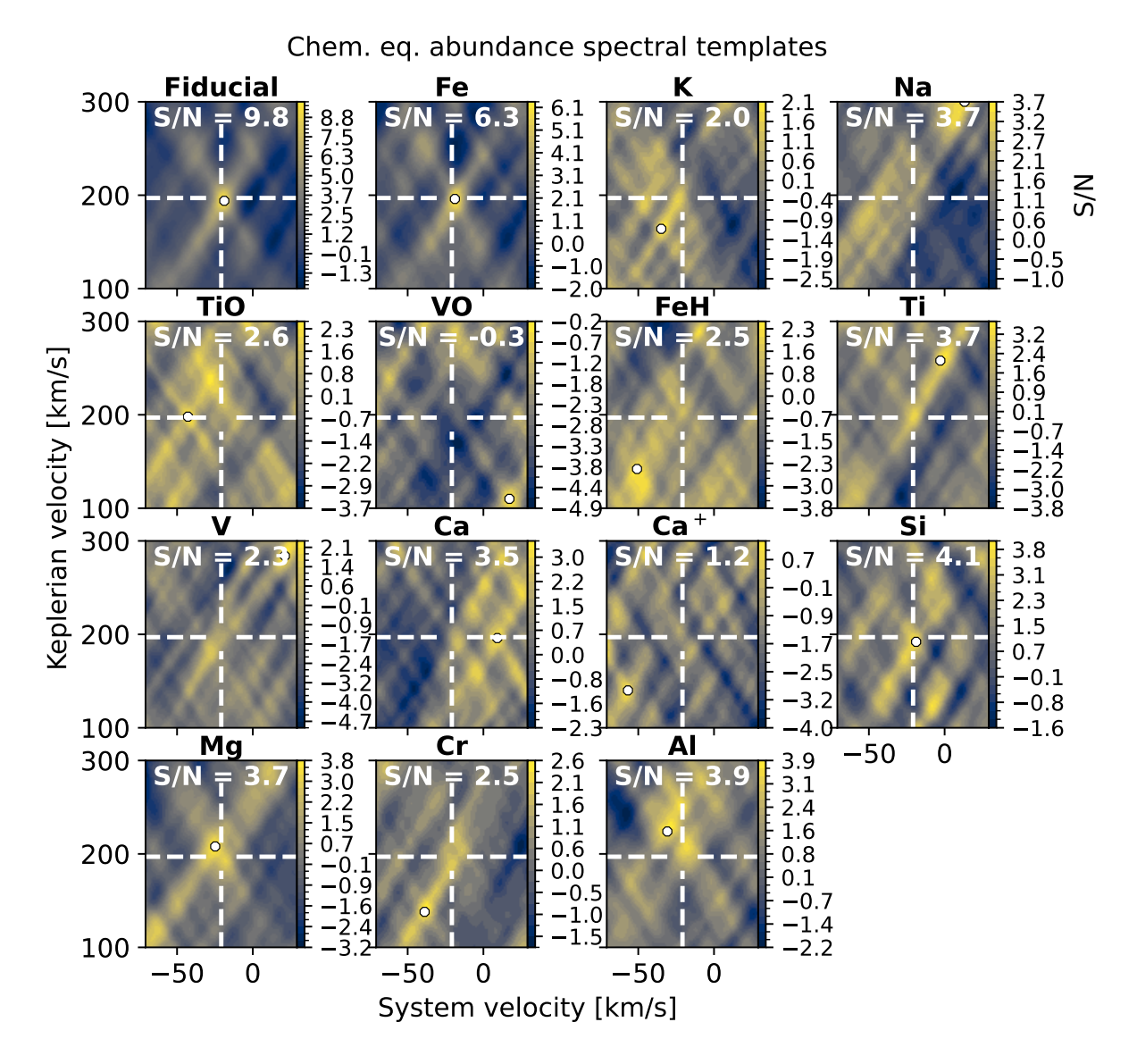


Figure 15. Similar to Fig 6, but shown for all the atmospheric species that have insignificant presence or absence.

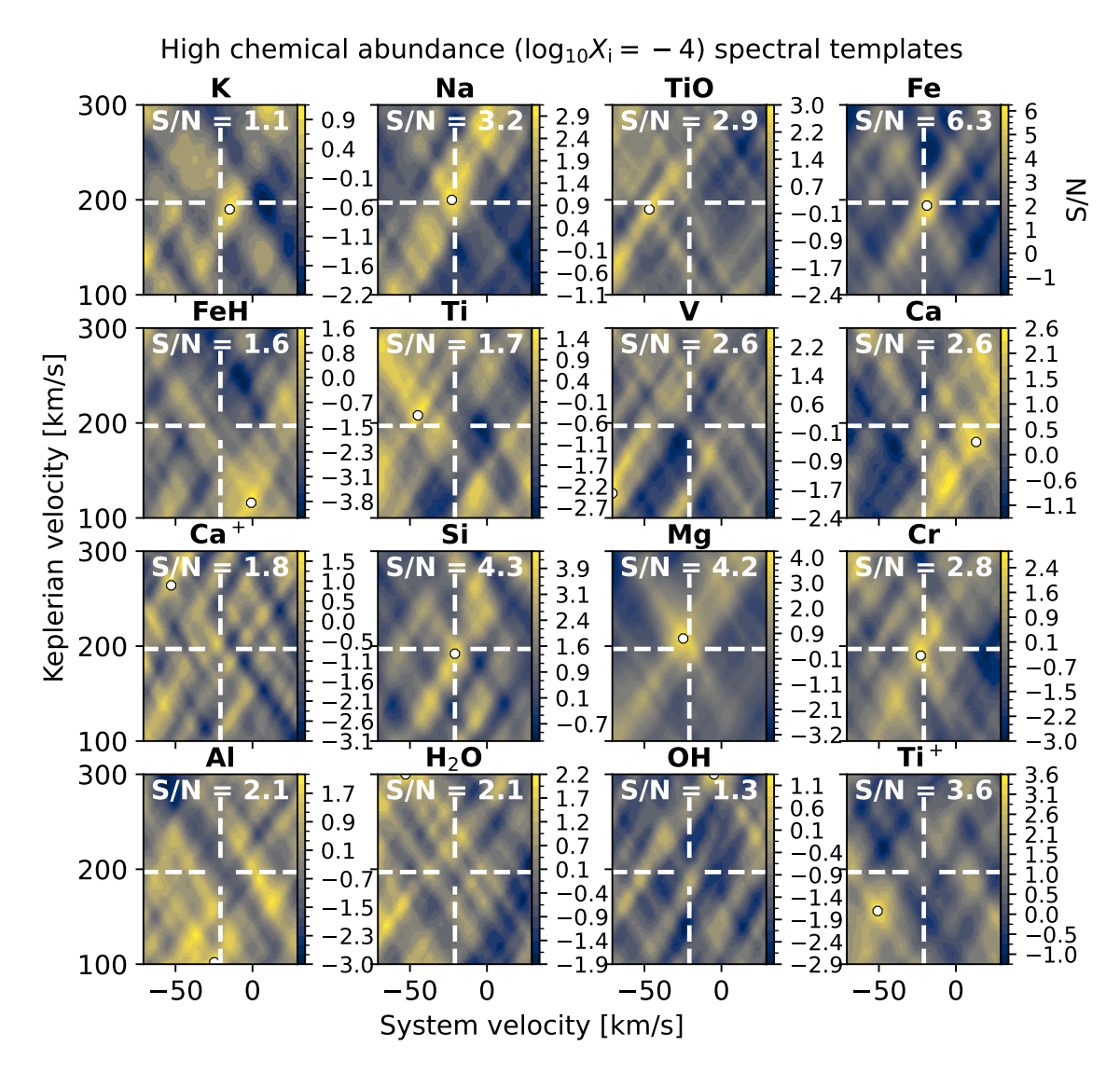


Figure 16. Similar to Fig 6, but shown for all spectral templates that included a single opacity source at an artificially high chemical abundance of  $\log_{10} VMR = -4$ .

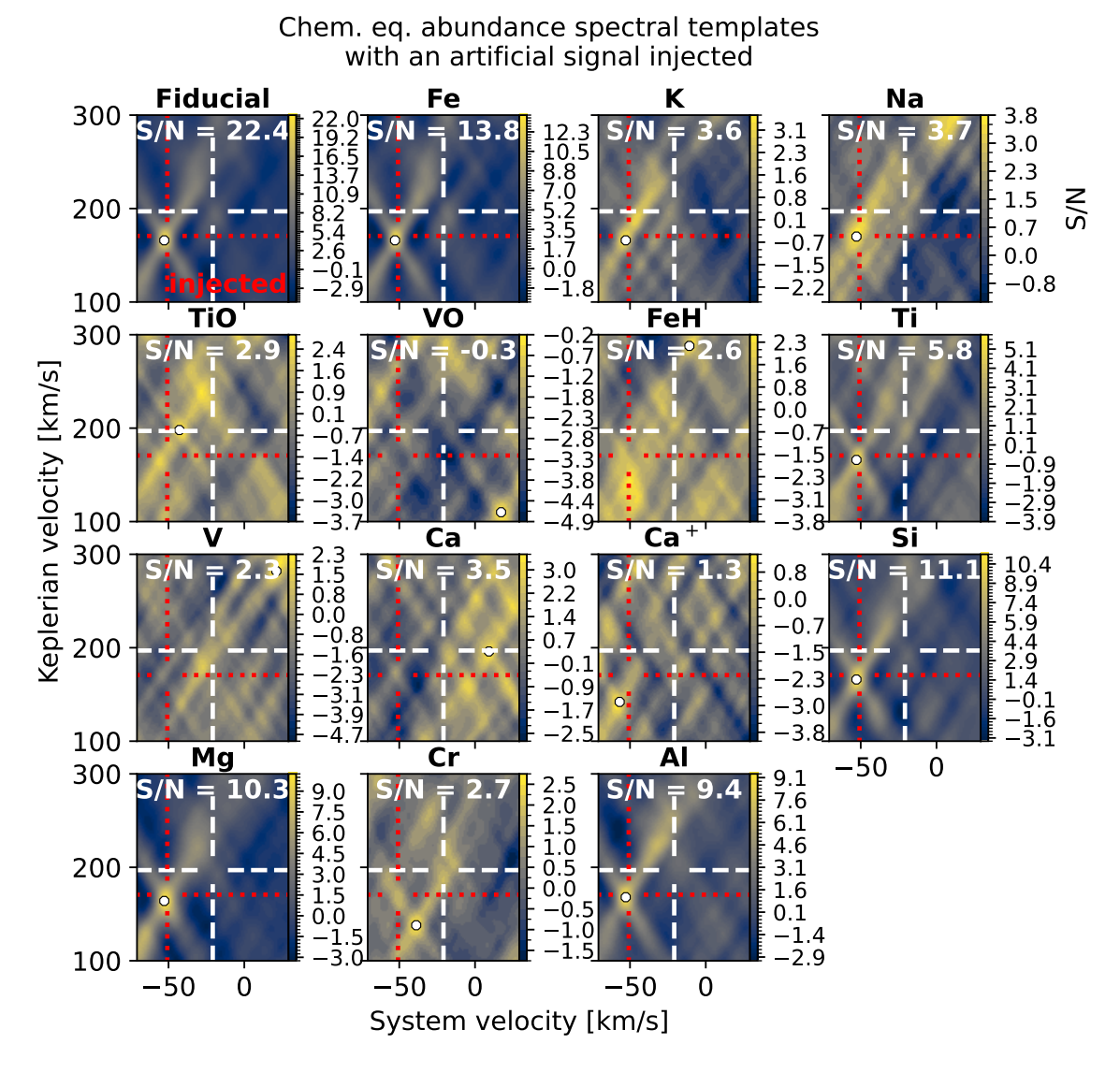


Figure 17. Similar to Fig 6, but shown for all the atmospheric species with an artificial exoplanet signal injected at a velocity offset of  $\Delta v_{\rm sys} = \Delta K_{\rm p} = -30$  km/s at nominal scale a=1. Recovery of the injected signal depends on the atmospheric species involved, where titanium (Ti) and iron (Fe) have the highest S/N detections at the injected velocity offset.

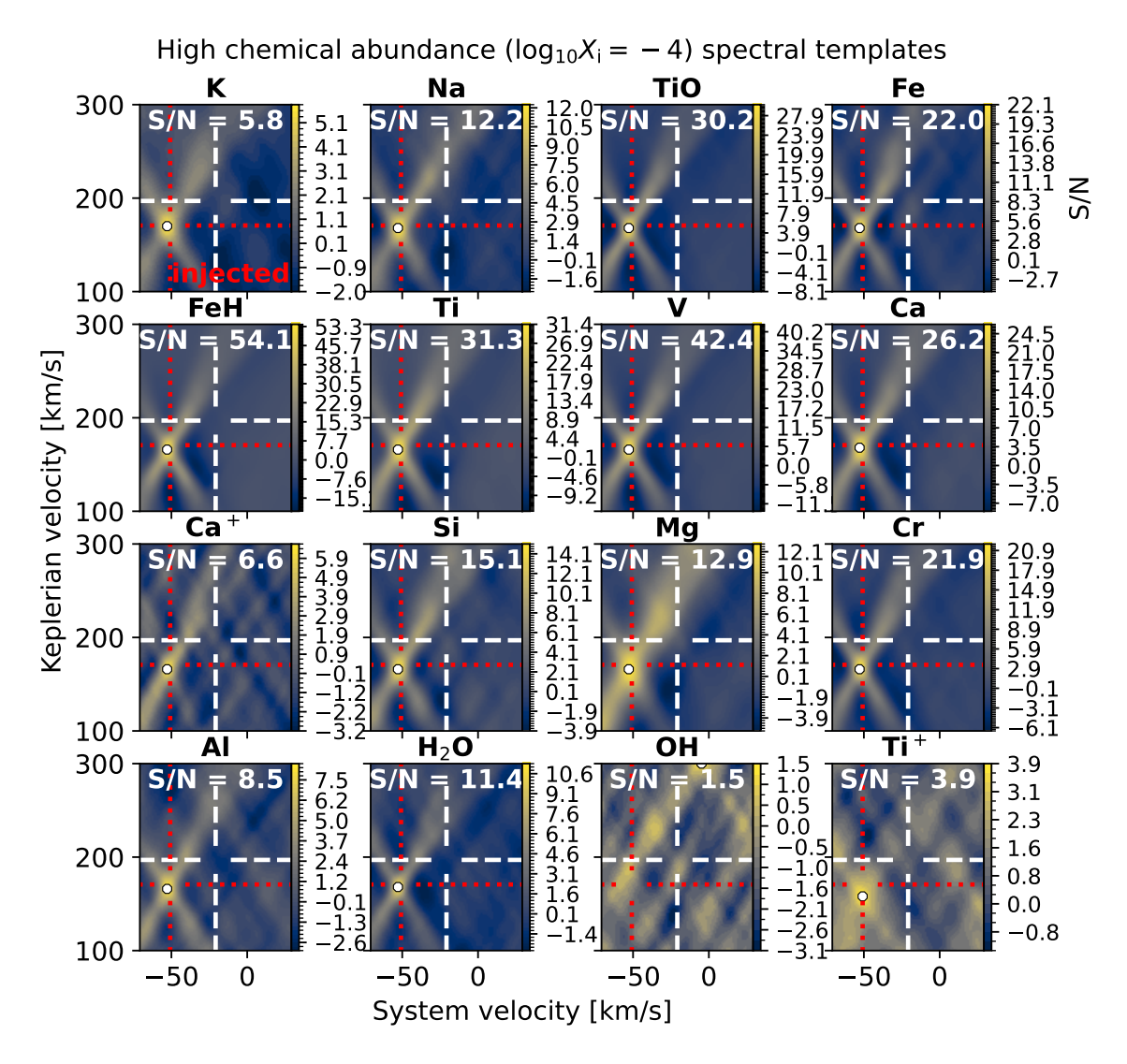


Figure 18. Similar to Fig 17, but shown for all spectral templates that included a single opacity source at an artificially high chemical abundance of  $\log_{10} VMR = -4$ .